Front. Mech. Eng. 2021, 16(1): 196–220
https://doi.org/10.1007/s11465-020-0609-z

RESEARCH ARTICLE

Laihao YANG, Zhu MAO, Shuming WU, Xuefeng CHEN, Ruqiang YAN

Nonlinear dynamic behavior of rotating blade with breathing crack

Abstract This study aims at investigating the nonlinear dynamic behavior of rotating blade with transverse crack. A novel nonlinear rotating cracked blade model (NRCBM), which contains the spinning softening, centrifugal stiffening, Coriolis force, and crack closing effects, is developed based on continuous beam theory and strain energy release rate method. The rotating blade is considered as a cantilever beam fixed on the rigid hub with high rotating speed, and the crack is deemed to be open and close continuously in a trigonometric function way with the blade vibration. It is verified by the comparison with a finite element-based contact crack model and bilinear model that the proposed NRCBM can well capture the dynamic characteristics of the rotating blade with breathing crack. The dynamic behavior of rotating cracked blade is then investigated with NRCBM, and the nonlinear damage indicator (NDI) is introduced to characterize the nonlinearity caused by blade crack. The results show that NDI is a distinguishable indicator for the severity level estimation of the crack in rotating blade. It is found that severe crack (i.e., a closer crack position to blade root as well as larger crack depth) is expected to heavily reduce the stiffness of rotating blade and apparently result in a lower resonant frequency. Meanwhile, the super-harmonic resonances are verified to be distinguishable indicators for diagnosing the crack existence, and the third-order super-harmonic resonances can serve as an indicator for the presence of severe crack since it only distinctly appears when the crack is severe.

Received May 1, 2020; accepted September 6, 2020

Laihao YANG (✉), Shuming WU, Xuefeng CHEN, Ruqiang YAN
The State Key Laboratory for Manufacturing Systems Engineering, Xi'an Jiaotong University, Xi'an 710049, China; School of Mechanical Engineering, Xi'an Jiaotong University, Xi'an 710049, China
E-mail: yanglaihao@xjtu.edu.cn

Zhu MAO
The Structural Dynamics and Acoustic Systems Laboratory, University of Massachusetts Lowell, Lowell, MA 01854, USA

Keywords rotating blade, breathing crack, nonlinear vibration, nonlinear damage indicator

1 Introduction

Rotating blades, one of the core components of rotating machines, are extensively applied in modern industry, such as gas turbines, jet engines, power plants, pumps, helicopters, and wind turbines. The blade-related failures (up to 42% of the total failures [1]) are often classified as the major sources of failures in many gas turbines since rotating blades suffer extreme operating conditions, such as high mechanical loading due to extreme changes in both temperature and pressure, high/low-cycle fatigue (HCF/LCF) loading, high centrifugal loading due to high spinning speed, and foreign object damage (FOD). One of the most common failure modes of rotating blades is crack, which is related to a variety of factors including FOD, HCF/LCF, manufacturing flaws, stress corrosion, ingested debris, and resonant fatigue [2]. For example, an F35A fighter caught fire during liftoff due to blade off of F135 engine which is induced by fatigue crack failure and accelerated by excessive blade-casing rubbing [3], and the Trent 1000 engine installed on Boeing 787-9 has been suffering from the severe blade crack problem caused by corrosion-related fatigue since 2016 [4].

Recent years have witnessed a growing interest in blade damage detection and an imperative need to develop an effective and robust blade health monitoring (BHM) technique to enhance the operational reliability and safety of the bladed rotating machines. Amongst all the conventional BHM techniques (such as, vibration analysis, acoustic emission, infrared thermography, strain gage measurements, and pressure field assessments) vibration analysis is the most popular since it provides the longest lead time to blades failure [5,6]. However, despite the advances in theory and technology of blade fault diagnosis over many years, effective and accurate measurement of blade vibration performance still encounters with some

significant challenges, which in turn triggers the need for further improvements on the comprehending of blade (with or without damage) vibration phenomenon [6].

Over the past decades, numerous interests and efforts are dedicated to the investigation on blade vibrations [7–9]. Some general dynamic models, including lumped-mass model [10], analytical model based on beam theory [11–13] and plate theory [14,15], and finite element (FE) model [16,17], have been proposed to predict the vibration behavior of rotating blades. Through numerical simulations, free vibration [14] and nonlinear behavior [11] of rotating blades considering the Coriolis effect, spinning softening and centrifugal stiffening effects, shaft-disc-blade coupling vibration [10–12], impact effects of shrouded blades [13,18], blade-casing rub-impact faults [16,19], blade-disk systems' mistuning [17,20], blade-off effects on the aero-engine vibration [21] are extensively investigated. Several vibration indicators for abnormal vibrations especially including those due to excessive blade-casing rubbing, vibration localization induced by mistuning, nonlinear effects owing to blade off, and sophisticated impact behavior caused by shrouded blades are found based on the existing dynamic models and numerical simulations. However, researches are seldom focused on the nonlinear effects of blade cracks which frequently result in gas turbine failures and further cause huge financial losses, including safety implications.

Cracks in mechanical structures have been facing significant difficulties in accurate modeling and effective detection because of its complexity, such as, various crack modes, sophisticated crack geometries, and nonlinear crack surface contacts [22]. By adopting the assumption of stationary blade, the linear and nonlinear dynamic behavior of blades (stationary cantilever beams) with crack are extensively studied. Several crack models including local compliance model (LFM) [23], strain energy release rate (SERR)-based model (SERRM) [24], wavelet-FE model (WFEM) [25], two-dimensional-FE model (2D-FEM) [26] and three-dimensional-FE model (3D-FEM) [27] have been proposed to predict the dynamic behavior of cracked beams.

In earlier researches, the crack was assumed as an open one, i.e., linear model. For example, the LFM [23] and SERRM [24] used for multiple cracks identification assumed crack effects as a constant stiffness reduction, and the WFEM [25] utilized for single crack localization dealt with the crack as an additional constant stiffness matrix to merit the continuity conditions. Amongst all the conventional researches based on linear crack models, most are focused on the free vibration of cracked beams and identify the crack through natural frequency shift and localization the intersection point of three different frequency contour lines [23–25]. For example, Liu et al. [28,29] investigated the effects of crack depth and location on the natural frequencies and mode shapes of the cantilever beam with open crack, indicating that the phenomenon of abrupt changes of single-level stationary wavelet transform decomposition detail coefficients of the normalized mode shapes for the cracked beam can serve as an indicator for crack identification and localization. Linear models pose many advantages since an integrated theoretical foundation makes it easy to obtain analytical solutions and extract crack features. However, owing to the sophisticated contact behavior between two crack surfaces during vibration, dynamic characteristics of a cracked beam are nonlinear rather than linear, which obstructs the application of conventional linear vibration analysis tools, such as modal analysis and harmonic response analysis and further adds challenges to crack detection.

The nonlinearity of cracks is introduced on account of the closing behavior of two crack surfaces, which assumes that the crack opens and closes alternately during vibration [30]. This phenomenon is also called "breathing effect" of cracks. Generally, there are two approaches to simulate the "breathing effect" of cracks, i.e., (i) analytical method, which is often based on LFM or SERRM [31–33]; (ii) numerical method, which is normally based on FE numerical simulation and contact theory [27,34,35]. The key to nonlinear crack models is to obtain the time-varying structural parameters (including stiffness, damping and excitation force) induced by cracks. As for analytical model, the most extensively adopted model is bilinear crack model which assumes there are two crack state configurations, i.e., fully open configuration and fully closed configuration, and the crack alternates between the fully closed configuration and fully open configuration during vibration [34]. Therefore, the crack breathing behavior is simulated by assuming that the system stiffness alternates within two piecewise stiffness coefficients, wherein one is corresponding to the fully open configuration and the other is related to the fully closed configuration. Considering the practical engineering, the crack does not always directly switch from one configuration to the other, and some transition states that the crack is neither fully open nor fully closed may exist. To more accurately simulate the crack breathing behavior, the bilinear model (BM) is further extended from a piecewise model to a continuous model assuming that the stiffness changes continuously from the fully open configuration to the fully closed configuration [32]. In view of this, some numerical models were proposed to better solve the above issue, among which the contact crack model are the most extensively applied [27,35–37]. For example, by assuming crack as a pair of two frictionless contact surfaces, nonlinear breathing behavior of cracks is simulated by 2D-FEM [35] and a mixed beam/solid 2D-FEM is proposed to reduce the computation time [27]. Based on the mixed beam/solid 2D-FEM, the effects of elastic-support on the vibration responses of cracked beam is explored [37]. To consider the simulation accuracy and, meanwhile, promote the computation efficiency, Liu and Jiang [38] derived a cracked hexahedral element to

simulate the breathing effect. By comparing the analytical models and numerical models, it is worth noting that analytical models may be less accurate than numerical models, but analytical models are much more efficient and easier to solve than numerical models. Also, most of the basic nonlinear dynamic characteristics can be captured by analytical models. Based on both analytical and numerical models, several vibration indicators have been found for the breathing cracks, where one of the most significant indicators is the super-harmonic resonance in the sub-critical region. However, amongst all the above-mentioned investigations, most consider the blade to be stationary, and few involve the effects of high-speed spinning of blade including spin softening and centrifugal stiffening on the cracked blade.

Some researchers explored the coupling effects of blade crack and high-speed spinning. For example, Kuang and Huang [39,40] proposed a cracked blade–disk model on the basis of SERRM to predict stability and the mistuning behavior of blade–disk systems. Later, Panigrahi and Pohit [41] put forward a model for the rotating cracked blade with functionally graded materials by assuming the crack to be an additional spring at the crack location which adds a local flexibility to the system stiffness of blade. However, in their model [39–41], the crack is assumed to be an open one, namely, the nonlinear effects of crack are neglected. To further analyzing the nonlinear vibration of rotating cracked blades, Kim et al. [42] developed a breathing model using the bilinear assumption of cracks to investigate the coupling effects of cracks and spinning. Nevertheless, the conventional modal analysis method is adopted in their research to predict the natural frequency of cracked blade, which in turn neglects the influence of nonlinear effects of cracks. On the basis of lumped-mass blade model and local flexibility crack model, Xu et al. [43,44] derived a nonlinear model of rotating blades with breathing crack to identify weak crack using vibration power flow analysis and predict the mistuning behavior of blade-disc system using conventional modal analysis. Since the lumped-mass blade model is simplified to a single-degree-freedom system, the accuracy of their model will be significantly reduced. In view of this, the FE method is employed, which significantly promote the model accuracy. For example, the FE-based contact crack model (FECCM) is used to investigate the nonlinear vibration and mistuning behavior of rotating blades with breathing crack [45], and the accuracy and efficiency are further promoted by introducing the cracked hexahedral element to simulate the breathing crack [38]. However, their investigations are mainly focused on the free vibration analysis and mistuning behavior prediction rather than the nonlinear vibration of rotating cracked blade. Motivated by the FECCM, a general model for the breathing crack of rotating blade is proposed on the basis of stress state at the crack section by Xie et al. [46]. However, the effects of blade radial deformation and Coriolis force are neglected which may leads to the accuracy decreasing.

In this paper, a novel nonlinear rotating cracked blade model (NRCBM) is derived on the basis of continuous beam vibration theory and strain energy release rate method. The FECCM and the extensively applied BM are employed to verify the validation of the proposed NRCBM. The nonlinear dynamic responses under different excitation parameters and crack parameters are then investigated using the proposed NRCBM. The remainder of this paper is organized as follows. In Section 2, the NRCBM is specifically formulated, where the rotating blade is simplified as a cantilever Euler beam which is fixed on a rigid rotating hub and the crack is considered as a breathing crack. The coupling effects of high-speed spinning effects including spinning softening effects, centrifugal stiffening effects and Coriolis effects and nonlinear breathing crack are considered in this model. In Section 3, both the FECCM and the BM are employed to verify the validation of the derived NRCBM. In Section 4, three cases are illustrated to present the effects of excitation load parameters and crack parameters (crack depths and crack locations) on the nonlinear responses of NRCBM. In Section 5, limitations of the proposed method are discussed. Finally, conclusions are drawn in Section 6.

2 Nonlinear dynamic model of rotating blade with breathing crack (NRCBM)

As shown in Fig. 1, the rotating blade that is fixed on a rotating rigid disk is simplified as a cantilever Euler beam with the uniform section. *OXYZ* denotes the inertial frame, $o^{\mathrm{r}}x^{\mathrm{r}}y^{\mathrm{r}}z^{\mathrm{r}}$ and $o^{\mathrm{b}}x^{\mathrm{b}}y^{\mathrm{b}}z^{\mathrm{b}}$ represent the rotational and local blade frames, respectively. The schematic of the blade deformation is presented in Fig. 1(c), where $o^{\mathrm{d}}x^{\mathrm{d}}y^{\mathrm{d}}z^{\mathrm{d}}$ is the local disk frame. Ignoring the effects of rotating shaft, $o^{\mathrm{d}}x^{\mathrm{d}}y^{\mathrm{d}}z^{\mathrm{d}}$ is the same with *OXYZ*. In this study, u, v, and w denote the displacements in span-wise, lateral, and chordwise directions of the blade, respectively.

The dynamic model of the rotating blade system is formulated based on the following assumptions:

1) The disk is assumed to be rigid and the vibrations of the disk and shaft are neglected.

2) The material of the blade is assumed to be isotropic and the constitutive relationship meets Hook's law.

3) The rotating blade is simplified as a cantilever Euler beam which rigidly fixed on the disk, thus the contact between blade and disk and the shear effect of the blade are neglected.

2.1 Dynamic model of rotating blade without crack

In $o^{\mathrm{r}}x^{\mathrm{r}}y^{\mathrm{r}}z^{\mathrm{r}}$, the position vector $\boldsymbol{r}$ of arbitrary blade point Q can be expressed as

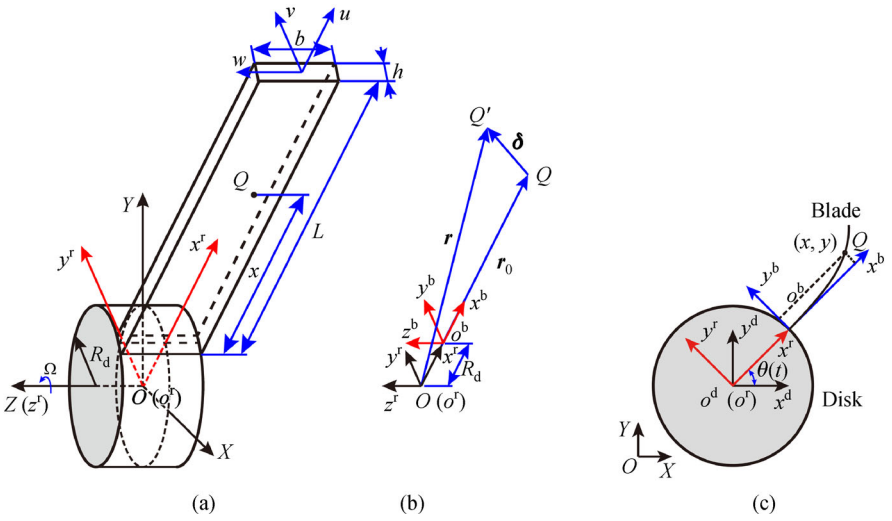

Fig. 1 (a) Schematic of the rotating blade; (b) motion of the blade; (c) schematic diagram of the blade deformation.

$$\boldsymbol{r} = \boldsymbol{r}_0 + \boldsymbol{\delta} = \begin{bmatrix} x + R_\mathrm{d} + u \\ y + v \\ z + w \end{bmatrix},$$

$$\boldsymbol{r}_0 = \begin{bmatrix} x + R_\mathrm{d} \\ y \\ z \end{bmatrix},$$

$$\boldsymbol{\delta} = \begin{bmatrix} u \\ v \\ w \end{bmatrix}, \tag{1}$$

where $\boldsymbol{r}_0$ is the initial position vector of point Q, and $\boldsymbol{\delta}$ denote the displacement vector caused by the deformation from point Q to point Q'. In this study, the membrane stretch in chordwise direction is ignored, i.e., $w = 0$. The velocity of point Q ($\boldsymbol{v}_Q$) can be calculated as

$$\boldsymbol{v}_Q = \dot{\boldsymbol{\delta}} + \overline{\boldsymbol{\Omega}} \times \boldsymbol{r} = \dot{\boldsymbol{\delta}} + \boldsymbol{\Omega}\boldsymbol{r}, \tag{2}$$

where

$$\overline{\boldsymbol{\Omega}} = \begin{bmatrix} \Omega_x \\ \Omega_y \\ \Omega_z \end{bmatrix},$$

$$\boldsymbol{\Omega} = \begin{bmatrix} 0 & -\Omega_z & \Omega_y \\ \Omega_z & 0 & -\Omega_x \\ -\Omega_y & \Omega_x & 0 \end{bmatrix},$$

$$\dot{\boldsymbol{\delta}} = \begin{bmatrix} \dot{u} \\ \dot{v} \\ 0 \end{bmatrix},$$

where $\overline{\boldsymbol{\Omega}}$ is the angular speed vector, and $\boldsymbol{\Omega}$ denotes the skew-symmetric matrix of $\overline{\boldsymbol{\Omega}}$.

Since the bladed-disk system rotates about z-axis, i.e., $\Omega_x = \Omega_y = 0$, and $\Omega_z = \Omega = 2\pi f_\Omega$, where f_Ω and Ω denote the rotating frequency and the angular speed of the blade–disk system, respectively. Then, $\boldsymbol{v}_Q$ can be rewritten as

$$\boldsymbol{v}_Q = \begin{bmatrix} \dot{u} \\ \dot{v} \\ 0 \end{bmatrix} + \begin{bmatrix} -\Omega v \\ \Omega(x + R_\mathrm{d} + u) \\ 0 \end{bmatrix} = \begin{bmatrix} \dot{u} - \Omega v \\ \dot{v} + \Omega(x + R_\mathrm{d} + u) \\ 0 \end{bmatrix}. \tag{3}$$

The kinetic energy of the blade (T_s) can be derived as

$$T_\mathrm{s} = \frac{1}{2}\int_0^L \rho \iint_A (\boldsymbol{v}_Q^\mathrm{T} \cdot \boldsymbol{v}_Q)\mathrm{d}A\mathrm{d}x, \tag{4}$$

where ρ, L, and A denote the density, length, and cross-section area of the blade, respectively.

Considering the centrifugal stiffening effect, the potential energy of the blade (V_s) is derived as

$$V_\mathrm{s} = V_\mathrm{s}^\mathrm{e} + V_\mathrm{s}^\Omega, \tag{5}$$

with

$$\begin{cases} V_{\mathrm{s}}^{\mathrm{e}} = \dfrac{1}{2}\displaystyle\int_0^L EA\left(\frac{\partial u}{\partial x}\right)^2 \mathrm{d}x + \frac{1}{2}\int_0^L EI\left(\frac{\partial^2 v}{\partial x^2}\right)^2 \mathrm{d}x, \\ V_{\mathrm{s}}^{\Omega} = \dfrac{1}{2}\displaystyle\int_0^L f_{\mathrm{c}}(x)\left(\frac{\partial v}{\partial x}\right)^2 \mathrm{d}x, \end{cases} \tag{6}$$

where $V_{\mathrm{s}}^{\mathrm{e}}$ denotes the strain energy due to the bending moment, V_{s}^{Ω} represents the strain energy due to the centrifugal force caused by the blade rotation, and E, I, and $f_{\mathrm{c}}(x)$ denote the Young's modulus, area moment of inertia, and centrifugal force, respectively.

As shown in Fig. 2, the centrifugal force of a micro-unit $\mathrm{d}x$ of the blade is

$$\mathrm{d}f_{\mathrm{c}}(x) = \mathrm{d}(mR\Omega^2) = \rho A\Omega^2(R_{\mathrm{d}} + x)\mathrm{d}x, \tag{7}$$

where m denotes the mass of the micro-unit, and R is the distance away from the centroid of the micro-unit to point o^{r}.

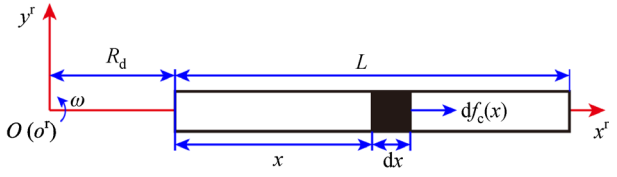

Fig. 2 Schematic of the centrifugal force for a micro-unit of the blade.

Then, the centrifugal force of blade is derived as

$$f_{\mathrm{c}}(x) = \int_x^L \mathrm{d}f_{\mathrm{c}}(x) = \rho\Omega^2\int_x^L A(R_{\mathrm{d}} + x)\mathrm{d}x. \tag{8}$$

Assume that the aerodynamic force $f_{\mathrm{e}}(x,t)$ is uniformly distributed along the blade length and perpendicular to the blade flatwise surface, and then the total virtual work done by $f_{\mathrm{e}}(x,t)$ is obtained as

$$W_{\mathrm{non}} = \int_x^L f_{\mathrm{e}}(x,t)v\mathrm{d}x, \tag{9}$$

with

$$f_{\mathrm{e}}(x,t) = F_0 + \sum_1^K F_{EO}\sin(EO\cdot\Omega t), EO \in \mathbb{R}^+, \tag{10}$$

where EO denotes the engine order, F_{EO} denotes the amplitude of the engine order excitation, and F_0 is the constant component of the excitation force. If $EO \in \mathbb{Z}^+$, the synchronous vibration of the blade will be excited, while if $EO \in \mathbb{R}^+ \cap EO \notin \mathbb{Z}^+$, the asynchronous vibration of the blade will be excited [47].

According to Hamilton principle, the dynamic equation of the blade can be obtained by

$$\delta\int_{t_1}^{t_2}(T_{\mathrm{s}} - V_{\mathrm{s}} + W_{\mathrm{non}})\mathrm{d}t = 0, \tag{11}$$

$$\begin{cases} \displaystyle\int_0^L \rho A\ddot{u}\mathrm{d}x - 2\int_0^L \rho A\Omega\dot{v}\mathrm{d}x - \int_0^L \rho A\Omega^2 u\mathrm{d}x - \int_0^L \rho A\dot{\Omega}v\mathrm{d}x \\ -\displaystyle\int_0^L EAu_x'' \ \mathrm{d}x = \int_0^L \rho A\Omega^2(x + R_{\mathrm{d}})\mathrm{d}x, \\ \displaystyle\int_0^L \rho A\ddot{v}\mathrm{d}x + 2\int_0^L \rho A\Omega\dot{u}\mathrm{d}x - \int_0^L \rho A\Omega^2 v\mathrm{d}x + \int_0^L \rho A\dot{\Omega}u\mathrm{d}x \\ +\displaystyle\int_0^L EAv_x^{(4)}\mathrm{d}x - \int_0^L \left(f_{\mathrm{c}}'(x)v_x' + f_{\mathrm{c}}(x)v_x''\right)\mathrm{d}x \\ = -\displaystyle\int_0^L \rho A\dot{\Omega}(x + R_{\mathrm{d}})\mathrm{d}x + \int_x^L f_{\mathrm{e}}(x,t)\mathrm{d}x, \end{cases} \tag{12}$$

with $\dot{u} = \dfrac{\partial u}{\partial t}$, $\ddot{u} = \dfrac{\partial^2 u}{\partial t^2}$, $u_x'' = \dfrac{\partial^2 u}{\partial x^2}$, and $u_x^{(4)} = \dfrac{\partial^4 u}{\partial x^4}$.

2.2 Discretization of differential equation

In this study, the blade deformations (see Eq. (12)) are discretized by using Galerkin method as

$$\begin{cases} u(x,t) = \displaystyle\sum_{i=1}^N \phi_{1i}(x)U_i(t), \\ v(x,t) = \displaystyle\sum_{i=1}^N \phi_{2i}(x)V_i(t), \end{cases} \tag{13}$$

where $U_i(t)$ and $V_i(t)$ are canonical coordinates corresponding to the longitudinal displacement $u(x,t)$ and the lateral displacement $v(x,t)$, respectively, $\phi_{1i}(x)$ and $\phi_{2i}(x)$ are the modal shape functions for longitudinal vibration and lateral vibration, respectively. According to vibration theory of continuous Euler beam, $\phi_{1i}(x)$ and $\phi_{2i}(x)$ are expressed as [13]

$$\begin{cases} \phi_{1i}(x) = \sin\dfrac{(2i-1)\pi x}{2L}, \\ \phi_{2i}(x) = \sin(\beta_i x) - \sinh(\beta_i x) \\ \qquad\qquad -\alpha_i\left(\cos(\beta_i x) - \cosh(\beta_i x)\right), \end{cases} \tag{14}$$

with $\alpha_i = \dfrac{\sin(\beta_i L) + \sinh(\beta_i L)}{\cos(\beta_i L) + \cosh(\beta_i L)}$, $i = 1, 2, \ldots, N$. Wherein N is the number of modal truncation and β_i is the eigenvalue of the equation $\cos(\beta_i L)\cosh(\beta_i L) = -1$. Substituting Eqs. (13) and (14) into Eq. (12), the differential equation of the uncracked blade can be obtained and expressed in matrix form as

$$\boldsymbol{M}_{\mathrm{b}}\ddot{\boldsymbol{q}} \ (\boldsymbol{G}_{\mathrm{b}} + \boldsymbol{D}_{\mathrm{b}})\dot{\boldsymbol{q}} + \boldsymbol{K}_{\mathrm{b}}\boldsymbol{q} = \boldsymbol{F}, \tag{15}$$

with $\boldsymbol{K}_{\mathrm{b}} = \boldsymbol{K}_{\mathrm{e}} + \boldsymbol{K}_{\mathrm{st}} + \boldsymbol{K}_{\mathrm{so}} + \boldsymbol{K}_{\mathrm{acc}}$. Wherein $\boldsymbol{q}$, $\boldsymbol{M}_{\mathrm{b}}$, $\boldsymbol{G}_{\mathrm{b}}$, $\boldsymbol{D}_{\mathrm{b}}$, $\boldsymbol{K}_{\mathrm{b}}$, and $\boldsymbol{F}$ are modal displacement vector, mass matrix, gyroscopic matrix, damping coefficients matrix, stiffness matrix, and the external force vector, respectively; $\boldsymbol{K}_{\mathrm{e}}$, $\boldsymbol{K}_{\mathrm{st}}$, $\boldsymbol{K}_{\mathrm{so}}$, and $\boldsymbol{K}_{\mathrm{acc}}$ are structural stiffness matrix, centrifugal stiffening matrix, spin softening matrix, and stiffness

caused by acceleration, respectively. The expressions of these matrices can be found in Appendix A.

2.3 Dynamic model of breathing crack

The schematic diagram of cracked blade is shown in Fig. 3. According to Ref. [48], alteration of the elastic deformation energy in presence of the crack caused by bending moment is the only significant change in the case of slender beams. Thus, the potential energy of the cracked blade consists of three terms:

$$V_{\mathrm{s}} = V_{\mathrm{s}}^{\mathrm{e}} + V_{\mathrm{s}}^{\Omega} - V_{\mathrm{s}}^{\mathrm{c}}, \tag{16}$$

where $V_{\mathrm{s}}^{\mathrm{c}}$ is the released energy of the crack. If the crack is initiated by the bending fatigue, the stress filed around the crack tip will be dominated by the mode I loading [24]. Only considering mode I loading, $V_{\mathrm{s}}^{\mathrm{c}}$ has the following form:

$$V_{\mathrm{s}}^{\mathrm{c}} = \int_{-h/2}^{h/2}\int_{0}^{a_{\mathrm{c}}} J\mathrm{d}a\mathrm{d}y = \int_{-h/2}^{h/2}\int_{0}^{a_{\mathrm{c}}} \frac{1-\nu^2}{E}K_{\mathrm{I}}^2\mathrm{d}a\mathrm{d}y, \tag{17}$$

where h is the thickness of blade, a_{c} denotes the crack depth, ν is the Poisson's ratio, $J = \dfrac{1-\nu^2}{E}K_{\mathrm{I}}^2$ is the strain energy density function, and K_{I} denotes the stress intensity factor under mode I loading. In the case of mode I loading, K_{I} can be approximated as [24,49]

$$K_{\mathrm{I}} = \frac{1}{2}Eh\nu_x''(l_{\mathrm{c}})\sqrt{\pi h\gamma}F_{\mathrm{I}}(\gamma), \tag{18}$$

with

$$F_{\mathrm{I}}(\gamma) = \sqrt{\frac{2}{\pi\gamma}\tan\frac{\pi\gamma}{2}}\frac{0.923 + 0.199\left(1-\sin\dfrac{\pi\gamma}{2}\right)^4}{\cos\dfrac{\pi\gamma}{2}}, \tag{19}$$

where the revision term $F_{\mathrm{I}}(\gamma)$ denotes the geometrical factor depending on relative crack depth $\gamma = a_{\mathrm{c}}/h$. Substitute Eqs. (18) and (19) into Eq. (17), and then we have

$$V_{\mathrm{s}}^{\mathrm{c}} = 3(1-\nu^2)Q(\gamma)h\int_0^L EI(\nu_{xx}'')^2\delta(x-l_{\mathrm{c}})\mathrm{d}x, \tag{20}$$

where $Q(\gamma) = \int_0^{\gamma}\pi\gamma F_{\mathrm{I}}^2(\gamma)\mathrm{d}\gamma$, l_{c} is the location of blade crack, and $\delta(x-l_{\mathrm{c}})$ is the delta function.

Similarly, the equation of motion for the blade with crack can be obtained.

$$\begin{cases} \displaystyle\int_0^L \rho A\ddot{u}\mathrm{d}x - 2\int_0^L \rho A\Omega\dot{v}\mathrm{d}x - \int_0^L \rho A\Omega^2 u\mathrm{d}x - \int_0^L \rho A\dot{\Omega}v\mathrm{d}x \\ \displaystyle -\int_0^L EAu_x''\mathrm{d}x = \int_0^L \rho A\Omega^2(x+R_{\mathrm{d}})\mathrm{d}x, \\ \displaystyle\int_0^L \rho A\ddot{v}\mathrm{d}x + 2\int_0^L \rho A\Omega\dot{u}\mathrm{d}x - \int_0^L \rho A\Omega^2 v\mathrm{d}x + \int_0^L \rho A\dot{\Omega}u\mathrm{d}x \\ \displaystyle +\int_0^L EIv_x^{(4)}\mathrm{d}x - \int_0^L \left(f_{\mathrm{c}}'(x)v_x' + f_{\mathrm{c}}(x)v_x''\right)\mathrm{d}x, \\ \displaystyle -6(1-\nu^2)Q(\gamma)h\int_0^L EIv_x^{(4)}\delta(x-l_{\mathrm{c}})\mathrm{d}x = \\ \displaystyle -\int_0^L \rho A\dot{\Omega}(x+R_{\mathrm{d}})\mathrm{d}x + \int_x^L f_{\mathrm{e}}(x,t)\mathrm{d}x. \end{cases} \tag{21}$$

Affected by the blade deflection, the crack will "open" and "close" alternately, namely, it will result in "breathing effect". The blade with closed crack is just like the uncracked blade, however, the open crack will reduce the blade stiffness. Namely, the "breathing effect" will further lead to the alternation of the blade stiffness. Herein, the breathing function $f_{\mathrm{breathing}}(t) = \left(1-\cos(\Omega t)\right)/2$ is utilized to describe the continuous "breathing effect" of the cracked blade. By coupling the "breathing effect", Eq. (15) can be rewritten as

$$\boldsymbol{M}_{\mathrm{b}}\ddot{\boldsymbol{q}} + (\boldsymbol{G}_{\mathrm{b}} + \boldsymbol{D}_{\mathrm{b}})\dot{\boldsymbol{q}} + \left(\boldsymbol{K}_{\mathrm{b}} - f_{\mathrm{breathing}}(t)\boldsymbol{K}_{\mathrm{cr}}\right)\boldsymbol{q} = \boldsymbol{F}, \tag{22}$$

where $\boldsymbol{K}_{\mathrm{cr}}$ is the stiffness alteration caused by fully "open" crack and given in Appendix B.

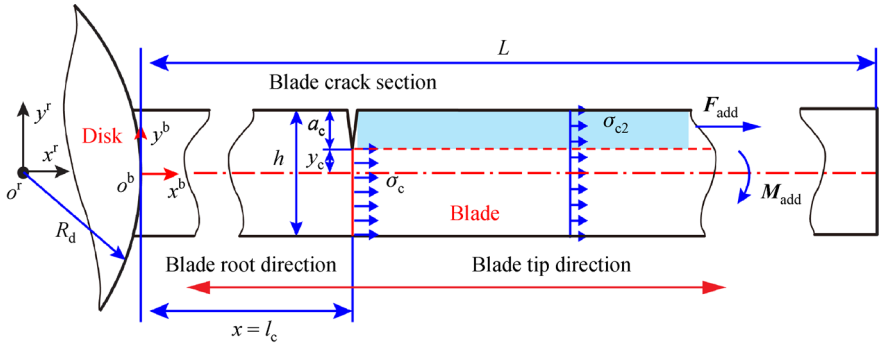

Fig. 3 Schematic diagram of the cracked blade.

3 Model verification

The geometrical and material parameters for numerical simulation are listed as follows:

Elasticity modulus: $E = 2 \times 10^{11}$ Pa;
Poisson's ratio: $v = 0.3$;
Blade density: $\rho = 7800$ kg/m^3;
Blade length: $L = 0.15$ m;
Blade width: $b = 0.04$ m;
Blade height: $h = 0.007$ m;
Disk radius: $R_d = 0.15$ m.

The validity of the proposed dynamic model of rotating cracked blade is verified by comparing among the results obtained by the proposed NRCBM, FECCM and BM.

3.1 FE-based contact crack model (FECCM)

In this section, the commercial FE software ANSYS 19.0 is employed to establish a 2D FE blade model with 8-node Plane 183 elements (plane stress state considering the thickness), as shown in Fig. 4. Since the influence of the friction between two crack interfaces is negligible, a frictionless contact model is used here [34]. In this study, the contact behavior of the crack interfaces is simulated by using the augmented Lagrangian method [34,36]. The same Rayleigh damping coefficients with that used in the proposed analytical model are utilized in the FE simulation. Newmark-β method is employed to solve the dynamic equation containing the nonlinear contact behavior.

3.2 Vibration of uncracked blade

In this subsection, the validity of the dynamic model for the rotating uncracked blade is verified by comparing both the natural frequencies and vibration responses which are respectively obtained by using FECCM and NRCBM with dimensionless relative crack depth $\gamma = 0$.

3.2.1 Comparison of natural frequencies

The free vibrations of uncracked blade are first compared by using the proposed analytical model and FE model and the results are shown in Table 1, where $f_{\mathrm{uFFM}i}$ and $f_{\mathrm{u}i}$ denote the natural frequency of normal blade obtained by FEM and NRCBM, respectively. It is worth noticing that errors under different rotating speeds are less than 1% for the first-order natural frequency, 2% for the second order natural frequency, and 3% for the third order natural frequency, which may not make a difference in engineering application. The comparative results indicate that the natural frequency obtained by the analytical model matches well with the one obtained by FEM, verifying the validity of the proposed dynamic model of uncracked blade.

The Campbell diagram of uncracked blade is further provided in Fig. 5 to present the natural vibration vs. rotating speed. It shows that the natural frequency increases with the increasing rotating speed because of the stiffening effect due to the spin of blade, which is also observed by Ma et al. [13] and Sinha and Turner [14]. As

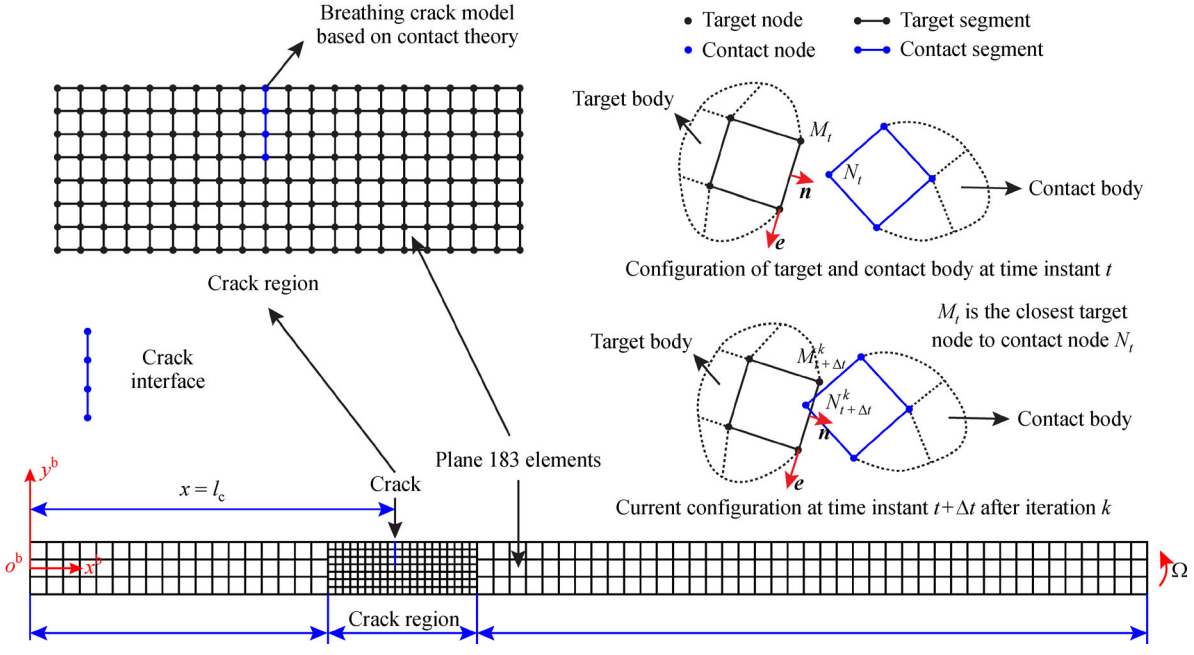

Fig. 4 FE model of the cantilever blade with breathing crack.

Table 1 Natural frequency of uncracked blade under different rotating speed

Modal order	Rotating speed, n/(r·min^{-1})	Natural frequency/Hz		Error/%
		$f_{\mathrm{uFFM}i}$	f_{ui}	
The first-order natural frequency	0	254.2	254.5	0.118
	5000	277.1	277.4	0.108
	10000	336.0	336.3	0.089
The second-order natural frequency	0	1577.1	1594.8	1.122
	5000	1607.5	1625.2	1.101
	10000	1695.1	1713.0	1.056
The third-order natural frequency	0	4347.9	4465.6	2.707
	5000	4380.1	4497.9	2.689
	10000	4475.2	4593.4	2.641

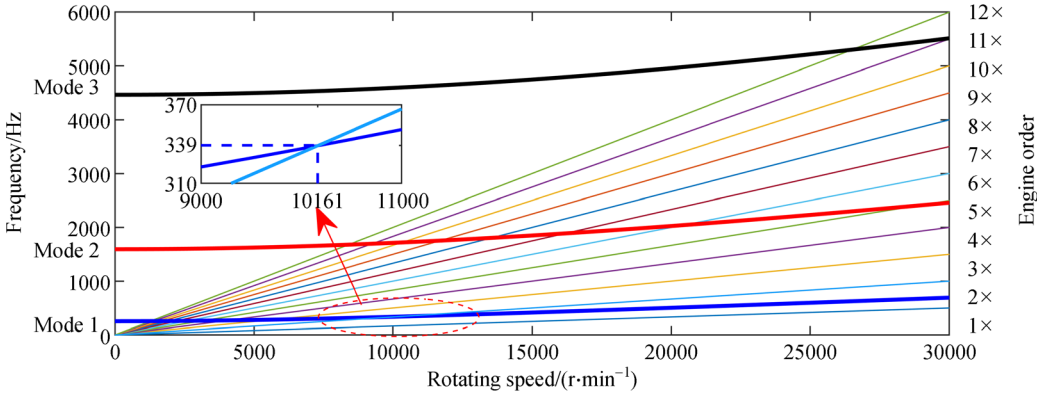

Fig. 5 Campbell diagram of the uncracked blade.

indicated in Fig. 5, the first-order resonant vibration will be excited at the rotating speed of 10161 r/min when $EO = 2$.

3.2.2 Comparison of vibration responses

The harmonic vibration responses of the normal blade obtained by FECCM and NRCBM with $\gamma = 0$ are first compared. The vibration responses are excited by the same harmonic force ($2000\sin(2\pi f_\omega t)$, $f_\omega = 80$ Hz) at the blade tip are shown in Fig. 6. It can be noted from Figs. 6(a) and 6(c) that, under stationary condition, the vibration responses obtained by NRCBM match well with those obtained by FECCM. The good agreement can also be observed among the results obtained by NRCBM and FECCM under rotational condition, as shown in Figs. 6(b) and 6(d). These observations indicate that the proposed NRCBM poses high accuracy enough for vibration prediction of rotating blade. By the way, because the absence of crack, both two systems established by FEM and analytical method, respectively, are linear rather than nonlinear, and thus only basic harmonic component (1×) can be observed in the response spectrums, as shown in Figs. 6(c) and 6(d). It is worth noting that the response amplitude under rotational condition is smaller than the one under stationary condition due to the stiffening effect.

3.3 Natural vibration of cracked blade

In this subsection, the validity of the proposed NRCBM is verified by comparing the natural frequencies and transient vibrations predicted by NRCBM with those predicted by FECCM. The natural vibration characteristics are further analyzed by comparing the prediction results of NRCBM and BM.

3.3.1 Comparison of vibration responses

Selecting the crack depth as 0.002 m, the impact vibration responses and amplitude–frequency responses (AFRs) under different rotating speeds are obtained and shown in Fig. 7. From Fig. 7, we can note that the impact vibration responses and AFRs obtained by NRCBM and FECCM match well with each other, especially under stationary condition.

For rotating blade, the crack open area cannot bear tensile force induced by centrifugal effect, thus an additional bending moment, attributed to the centrifugal effect of the subsection from crack surface to blade tip

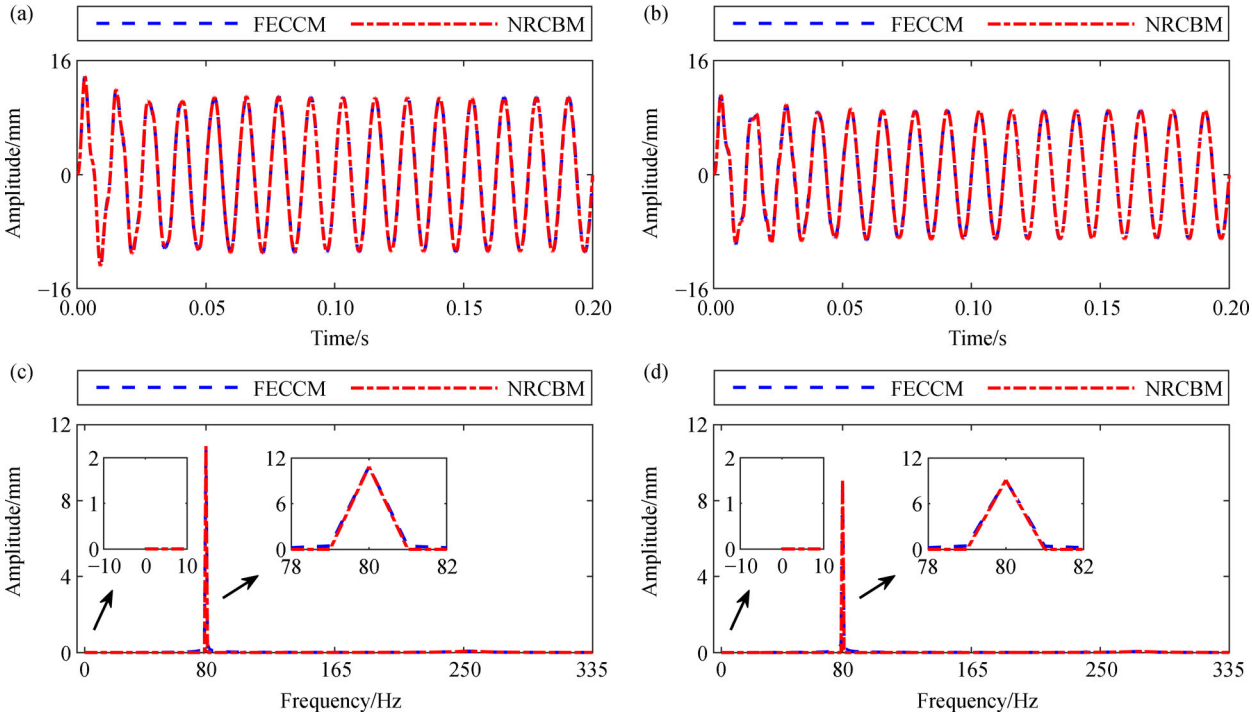

Fig. 6 Comparison of the harmonic vibration responses for uncracked blade, harmonic vibration responses at (a) 0 r/min and (b) 4800 r/min, spectrums at (c) 0 r/min and (d) 4800 r/min. FECCM: Finite element-based contact crack model; NRCBM: Nonlinear rotating cracked blade model.

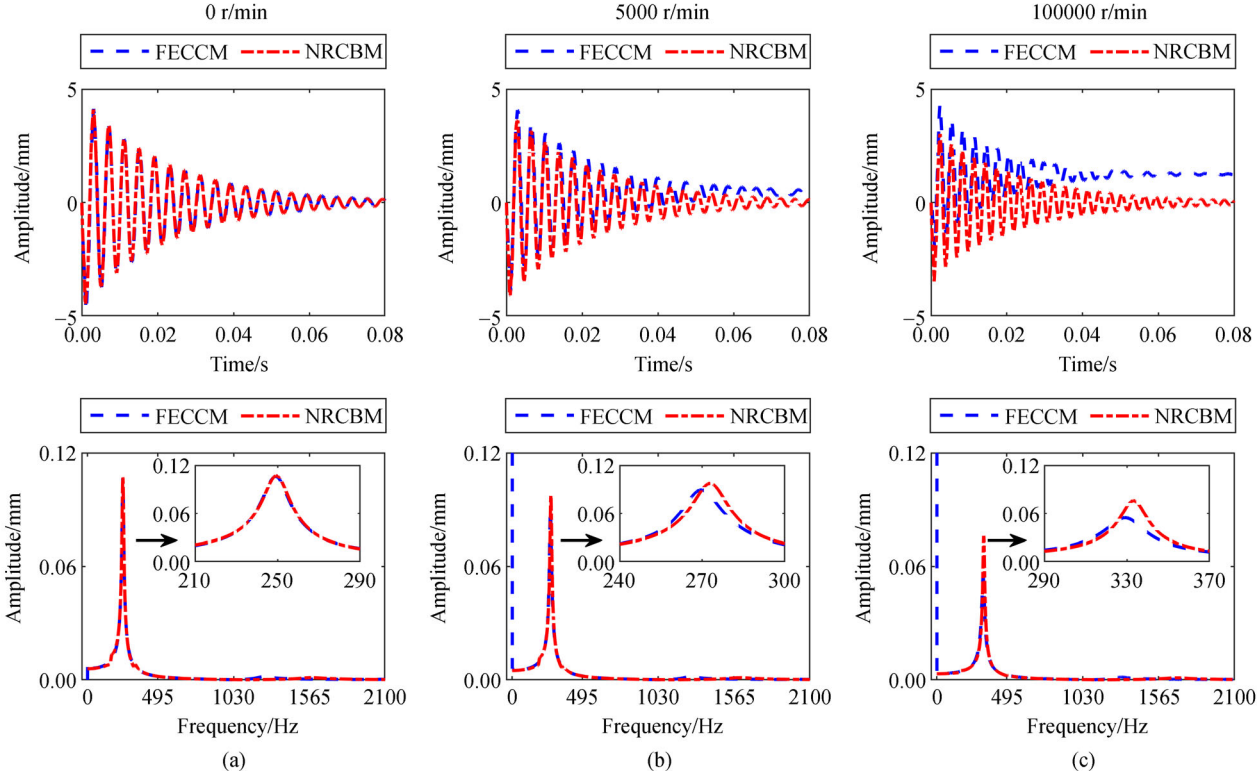

Fig. 7 The transient vibration responses and AFRs under different rotating speed: (a) 0 r/min, (b) 5000 r/min, and (c) 10000 r/min. AFR: Amplitude–frequency responses.

($l_c \leqslant x \leqslant L$) of the cracked blade, will be induced at the crack surface. As a result, an DC-component appears in the transient vibration responses (see Fig. 7(b)) obtained by FECCM due to the additional bending moment caused by rotating cracked blade, and it increases with the increasing speed. Without considering the additional bending moment in NRCBM, no DC-component occurs in the impact vibration responses obtained by NRCBM. The peak amplitudes of the AFRs under rotational conditions obtained by FECCM are smaller than that obtained by NRCBM due to presence of additional bending moment. The impact vibration responses with DC removed are further presented in Fig. 8, which indicates a good agreement between the FECCM results and NRCBM results. In this study, the additional bending moment is neglected because of our focus on the nonlinear behavior of rotating cracked blade and the difficulty in its accurate estimation.

Further, since the open crack cannot provide centrifugal tensile stress due to the discontinuity of the blade at crack surface, the strain energy of cracked blade induced by the centrifugal force differs from that of normal blade. The stiffening effect due to high-speed spin will also be weakened by the absence of materials at the crack section. Namely, the stiffness ($\boldsymbol{K}_{st}$) induced by centrifugal stiffening effect is reduced. The weakening of $\boldsymbol{K}_{st}$ is also neglected in NRCBM since it is the localized effect and hard to be accurately assessed, that's why the natural frequency (frequency value at the peak of AFRs) obtained by NRCBM are little smaller than that obtained by FECCM under rotational conditions. The natural frequency errors will further be analyzed in the following subsection 3.3.2.

As stated above, both the additional bending moment and the weakening effect of $\boldsymbol{K}_{st}$ are negligible, and thus both are neglected in NRCBM. To further verify this point of view, the harmonic vibration responses and their spectrums of cracked blade under stationary and rotational conditions are compared and the results are shown in Fig. 9. The vibration responses are obtained by applying a harmonic excitation force at the blade tip. Obviously, the results obtained by NRCBM agree well with the results obtained by FECCM, which verifies the validity of the proposed NRCBM. It is worth further noticing that the response amplitudes under rotational condition are smaller than that under stationary condition because the system's stiffness is increased by the stiffening effect due to blade spinning. By comparing the results in Fig. 6 and the ones in Figs. 9(a) and 9(b), we find that the presence of nonlinearity due to "breathing crack" induces super-harmonic components (such as 2×) in the spectrums. Although DC-components under rotational condition for FECCM are induced by the additional bending moment due to centrifugal effect, as shown in Fig. 9(c), which may introduce some small but acceptable differences between the results of FECCM and the ones of NRCBM. However, the general vibration characteristics obtained by both FECCM and NRCBM match well with each other.

3.3.2 Comparison of natural frequencies

In this subsection, the natural frequencies are compared among the results obtained by FECCM, NRCBM and BM. The "breathing effect" are involved in both FECCM and NRCBM. Since the nonlinear effect is coupled in both NRCBM and FECCM, traditional modal analysis method fails to present the natural vibration behavior of the blade with breathing crack. Thus, impact vibration responses, as shown in Fig. 7, are employed to acquire the natural vibration of the cracked blade through applying an impact force at the tip of the blade.

1) Comparison with the results of FECCM

In this case, the natural frequencies of rotating cracked blade obtained by FECCM and NRCBM are first compared. The first-order natural frequencies of the blades with different crack depths and rotating speeds are presented in Table 3. The relative errors between the results of FECCM and NRCBM are defined as

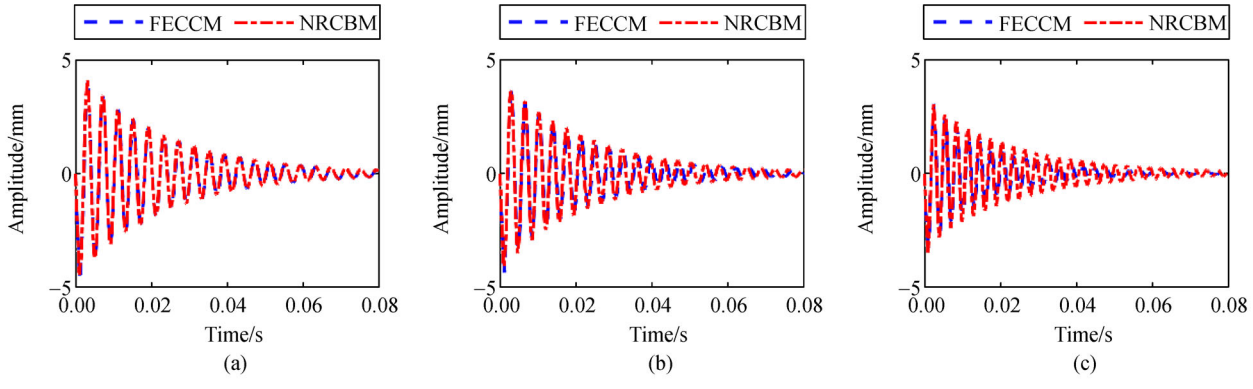

Fig. 8 The impact vibration response with mean removed under different rotating speeds: (a) 0 r/min, (b) 5000 r/min, and (c) 10000 r/min. FECCM: Finite element-based contact crack model; NRCBM: Nonlinear rotating cracked blade model.

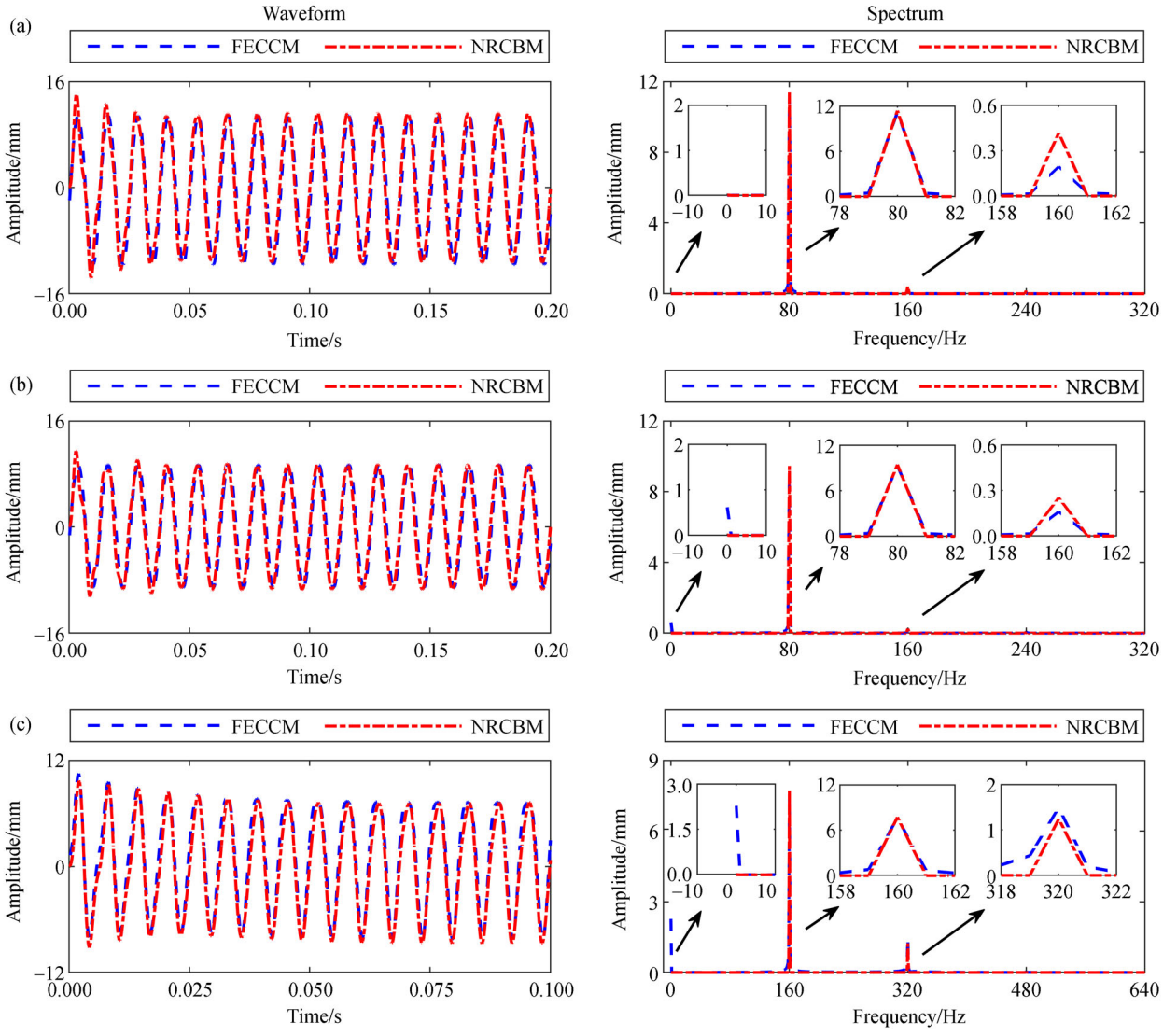

Fig. 9 The harmonic vibration responses and spectrums under different rotating speeds: (a) 0 r/min, (b) 4800 r/min, and (c) 9600 r/min. FECCM: Finite element-based contact crack model; NRCBM: Nonlinear rotating cracked blade model.

$$Error = \frac{(f_{ci} - f_{cFFMi})}{f_{cFFMi}} \times 100\%, \tag{23}$$

where f_{ci} and f_{cFFMi} denote the ith order natural frequencies obtained by NRCBM and FECCM, respectively.

The comparison of natural vibrations of cracked blade in Table 2 and Fig. 7 demonstrate that the results obtained by NRCBM agree well with that obtained by FECCM. It is worth noticing that the errors of the first-order natural frequency are less than 1% under most low-speed conditions and the maximum error is less than 3% under high-speed conditions, which could be accepted in practical engineering application.

The relative errors are further analyzed in Fig. 10. Because of the model errors, the relative errors under stationary condition vary from 0.7143% to –1.6260% as the crack depth changes from 0.001 to 0.003 m. It is implicated that the results of NRCBM will get smaller and smaller than that of FECCM with the increasing crack depth. However, under rotational conditions, the relative errors become larger when rotating speed increases. It is indicated that the results obtained by NRCBM get closer to that obtained by FECCM for a relatively deep crack (e.g., $a_c = 0.003$ m) with the increase of rotating speed (see from 0 to 5000 r/min). As the rotating speed increases continuously, the results of NRCBM will get larger than that of FECCM (see from 10000 to 15000 r/min). This phenomenon is attributed to that the weakening effect of centrifugal stiffness which is overlooked in NRCBM but involved in FECCM.

2) Comparison with the results of BM

In this case, the natural frequencies of rotating cracked

Table 2 Natural frequency of the cracked blade

Rotating speed, n /(r·min^{-1})	Crack depth, a_c/m	Natural frequency/Hz		Error/%
		f_{cFFMi}	f_{ci}	
0	0.001	252.0	253.8	0.7143
	0.002	250.0	249.7	–0.1200
	0.003	246.0	242.5	–1.6260
5000	0.001	274.0	276.0	0.7299
	0.002	271.0	273.0	0.5535
	0.003	264.0	263.5	–0.3788
10000	0.001	332.0	336.0	1.2048%
	0.002	330.0	332.5	1.0638
	0.003	326.0	327.0	0.6079
15000	0.001	405.0	414.0	2.2222
	0.002	404.0	413.3	2.3020
	0.003	401.0	409.0	1.9950

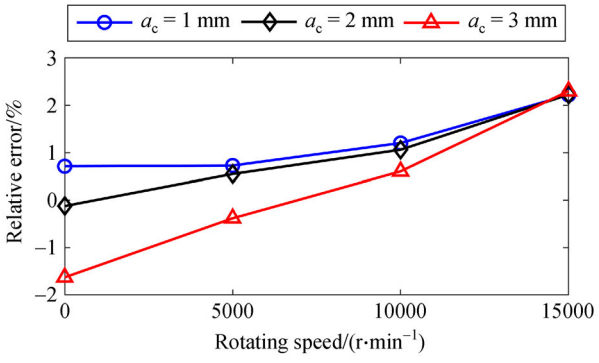

Fig. 10 Relative errors of the natural frequency obtained by FECCM and NRCBM, respectively. FECCM: Finite element-based contact crack model; NRCBM: Nonlinear rotating cracked blade model.

blades are further analyzed by comparing the results obtained by NRCBM and BM, respectively. The bilinear frequency was originally introduced to extract the exact natural frequency for a piecewise linear, single degree of freedom (SDOF) system. The bilinear frequency was then applied to predict the nonlinear vibration frequencies of cracked beams (SDOF system) by assuming that cracked beam has only two linear systems associated with two crack configurations, i.e., fully open configuration and fully closed configuration [50]. It was further extended to estimate the bilinear resonant frequency of mutil-degree of freedom cracked plate by Saito et al. [51]. The bilinear resonant frequency is verified (by Ma et al. [36] with FEM simulations and Andreaus and Baragatti [35] with experiments) to be accurate for systems with a relatively shallow crack. As described in Ref. [51], the ith bilinear resonant frequency of the cracked blade (f_{bi}) can be defined as:

$$f_{bi} = \frac{2f_{1i}f_{2i}}{f_{1i} + f_{2i}}, \tag{24}$$

where f_{1i} and f_{2i} denote the resonant frequencies of ith mode under the fully open configuration and the fully closed configuration, respectively. Selecting the rotating speed as 10000 r/min, the 1st order resonant frequencies of the cracked blade with different crack parameters (relative crack depth (γ) and relative crack location (ζ)) obtained by NRCBM and BM are listed in Tables 3 and 4, respectively, and compared in Fig. 11. It is indicated that the results obtained by NRCBM agree well with the results estimated by BM, especially when the crack is relatively shallow. The relative error between f_{bi} and f_{ci} slightly increases with the increasing γ and decreasing ζ for systems with shallow crack. However, when the relative crack depth is pretty large, meanwhile, the relative crack location approaches to the blade root, e.g., $\gamma = 0.5$ and $\zeta = 0.1$, the error between f_{bi} and f_{ci} gets relatively large (7.04%). Moreover, in the case of ($\gamma = 0.5, \zeta = 0.1$), the 1st order resonant frequency estimated by FECCM is 299 Hz, which means the result obtained by NRCBM is more accurate than BM for systems with a deep crack [51]. The comparative results indicate that both NRCBM and BM can accurately predict the first-order resonant frequency of the rotating blade with a relatively shallow crack, while the NRCBM prediction will be much more accurate than the BM prediction for the rotating blade with a relatively deep crack.

3.4 Summary of model verification

The comparative results among NRCBM, FECCM, and BM well verify the validity of the proposed NRCBM.

1) Under stationary conditions, the prediction results of NRCBM and FECCM are consistent with each other. For rotating blades, some negligible differences may appear

Table 3 Natural frequency of the cracked blade with different relative crack depths and locations obtained by NRCBM

Relative crack depth γ	Natural frequency/Hz									
	ζ = 0.1	ζ = 0.2	ζ = 0.3	ζ = 1/3	ζ = 0.4	ζ = 0.5	ζ = 0.6	ζ = 0.7	ζ = 0.8	ζ = 0.9
0.00	336.3	336.3	336.3	336.3	336.3	336.3	336.3	336.3	336.3	336.3
0.05	335.5	336.0	336.0	336.0	336.0	336.0	336.0	336.0	336.0	336.0
0.10	335.0	335.5	335.5	335.5	335.5	336.0	336.0	336.0	336.0	336.0
0.15	333.5	334.5	335.0	335.0	335.5	335.5	336.0	336.0	336.0	336.0
0.20	331.5	333.0	334.5	334.5	335.0	335.5	336.0	336.0	336.0	336.0
0.25	329.0	331.5	333.5	334.0	334.5	335.0	335.5	336.0	336.0	336.0
0.30	325.0	329.5	332.0	333.0	334.0	335.0	335.5	336.0	336.0	336.0
0.35	320.0	326.5	330.0	331.0	333.0	334.5	335.0	335.5	336.0	336.0
0.40	313.0	323.0	327.5	329.0	331.5	333.5	334.5	335.5	336.0	336.0
0.45	302.5	317.5	323.0	325.0	329.0	332.5	334.0	335.0	336.0	336.0
0.50	284.5	309.5	315.5	318.0	324.5	330.5	332.5	334.0	335.5	336.0

Note: $\gamma = a_c/h$, $\zeta = l_c/L$.

Table 4 Natural frequency of the cracked blade with different relative crack depths and locations estimated by BM

Relative crack depth, γ	Natural frequency/Hz								
	ζ = 0.1	ζ = 0.2	ζ = 0.3	ζ = 0.4	ζ = 0.5	ζ = 0.6	ζ = 0.7	ζ = 0.8	ζ = 0.9
0.00	336.3	336.3	336.3	336.3	336.3	336.3	336.3	336.3	336.3
0.05	336.0	336.2	336.2	336.3	336.3	336.3	336.3	336.3	336.3
0.10	335.2	335.6	335.9	336.1	336.2	336.3	336.3	336.3	336.3
0.15	333.8	334.8	335.4	335.8	336.1	336.2	336.3	336.3	336.3
0.20	331.8	333.6	334.7	335.4	335.9	336.1	336.2	336.3	336.3
0.25	328.9	331.9	333.7	334.9	335.6	335.9	336.2	336.3	336.3
0.30	324.9	329.7	332.2	334.1	335.2	335.7	336.1	336.3	336.3
0.35	319.0	326.6	330.0	332.9	334.6	335.4	335.9	336.2	336.3
0.40	310.1	322.3	326.7	331.1	333.7	334.8	335.7	336.2	336.3
0.45	295.2	316.0	321.0	328.1	332.3	333.8	335.1	336.1	336.3
0.50	265.8	306.0	309.5	322.1	329.8	331.4	333.6	336.0	336.3

Note: $\gamma = a_c/h$, $\zeta = l_c/L$.

between the results of NRCBM and FECCM due to the additional bending moment caused by centrifugal effects and the centrifugal stiffness reduction induced by crack opening, which is acceptable in practical engineering. In view of this, the additional bending moment is neglected in this study since it is difficult to be accurately modeled by using analytical method and the basic nonlinear dynamic behavior can be characterized by the proposed NRCBM.

2) For shallow cracks, both NRCBM and BM can well predict the first-order natural frequency of the rotating cracked blades, while the NRCBM prediction will be much more accurate than the BM estimation for a relatively deep crack.

4 Dynamic responses of NRCBM

In this section, three cases are selected to analyze the effect of excitation loads and crack parameters on the dynamic responses of NRCBM, and these parameters are presented in Table 5.

Sweep frequency test is utilized to obtain the overall dynamic behavior of NRCBM under certain rotating speed ranges. The rotating blade are excited by forces near three special frequency regions, i.e., super-harmonic resonant region ($f_{c1}/2$), primary resonant region (f_{c1}), and sub-harmonic resonant region ($2f_{c1}$). The sweep frequency interval is set as 1 Hz. Spectrum cascades are employed to compare the frequency-domain features under different parameters. Phase portraits are selected to characterize the nonlinear behavior of NRCBM under different parameters. As can be seen in Section 2.4, the rotating speed mainly influence the natural frequency of NRCBM. In this section, the rotating speed is selected as the 10000 r/min, where the natural frequency of the uncracked blade is 336.3 Hz and the natural frequency of cracked blade varies from 284.5 to

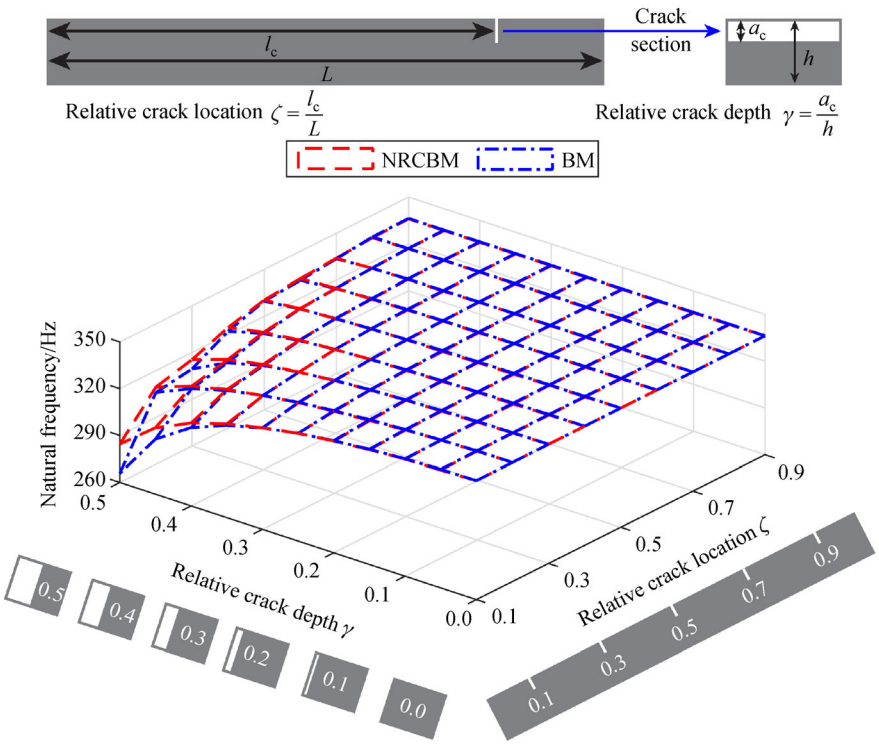

Fig. 11 Comparison of the first-order resonant frequency obtained by NRCBM and BM, respectively. NRCBM: Nonlinear rotating cracked blade model; BM: Bilinear model.

Table 5 Condition and crack parameters for the numerical simulation of NRCBM

Influence factors	Invariant parameters	Varying parameters
EO (Case 1)	$(\gamma,\ \zeta,\ F_{EO}) = (0.3,\ 1/3,\ 2000\ \mathrm{N})$	$EO = 1,\ 2,\ ...,\ 4$
	$(\gamma,\ \zeta,\ F_{EO}) = (0.5,\ 1/3,\ 2000\ \mathrm{N})$	$EO = 1,\ 2,\ ...,\ 4$
	$(\gamma,\ \zeta,\ F_{EO}) = (0.5,\ 2/3,\ 2000\ \mathrm{N})$	$EO = 1,\ 2,\ ...,\ 4$
γ (Case 2)	$(\zeta,\ EO,\ F_{EO}) = (1/3,\ 1,\ 2000\ \mathrm{N})$	$\gamma = 0.10,\ 0.15,\ ...,\ 0.50$
	$(\zeta,\ EO,\ F_{EO}) = (1/3,\ 2,\ 2000\ \mathrm{N})$	$\gamma = 0.10,\ 0.15,\ ...,\ 0.50$
	$(\zeta,\ EO,\ F_{EO}) = (1/3,\ 3,\ 2000\ \mathrm{N})$	$\gamma = 0.10,\ 0.15,\ ...,\ 0.50$
	$(\zeta,\ EO,\ F_{EO}) = (1/3,\ 4,\ 2000\ \mathrm{N})$	$\gamma = 0.10,\ 0.15,\ ...,\ 0.50$
ζ (Case 3)	$(\gamma,\ EO,\ F_{EO}) = (0.5,\ 1,\ 2000\ \mathrm{N})$	$\zeta = 0.10,\ 0.15,\ ...,\ 0.90$
	$(\gamma,\ EO,\ F_{EO}) = (0.5,\ 2,\ 2000\ \mathrm{N})$	$\zeta = 0.10,\ 0.15,\ ...,\ 0.90$
	$(\gamma,\ EO,\ F_{EO}) = (0.5,\ 3,\ 2000\ \mathrm{N})$	$\zeta = 0.10,\ 0.15,\ ...,\ 0.90$
	$(\gamma,\ EO,\ F_{EO}) = (0.5,\ 4,\ 2000\ \mathrm{N})$	$\zeta = 0.10,\ 0.15,\ ...,\ 0.90$

360 Hz when $\gamma \in [0.1,\ 0.5]$ and $\zeta \in [0.1,\ 0.9]$. Since it is close to the first-order critical frequency 339 Hz, the critical vibration may be excited when $EO = 2$.

In this study, to quantify the nonlinear effect of crack, a nonlinear damage indicator (NDI) is introduced. Herein, the NDI (h_r) is defined as the relative amount of magnitude (H_s) of super- or sub-harmonic components ($2\times$, $1/2\times$, ...) with respect to the amplitude of the basic harmonic component (H_b) [35]. The NDI is assessed as

$$h_r = \frac{H_s}{H_b}. \tag{25}$$

4.1 Effect of excitation loads

In this section, the effects of excitation frequency on the nonlinear vibration of rotating cracked blade are explored.

4.1.1 Case 1: Effects of excitation frequency

In this section the effects of excitation frequency on the system dynamic responses will be investigated. Harmonic response analysis is performed under the frequency range from 50 (3000 r/min) to 750 Hz (45000 r/min) with an interval of 1 Hz (60 r/min), which covers the super-harmonic, primary, and sub-harmonic resonant regions. The general dynamic behavior of rotating blade with breathing crack under different excitation frequency is first analyzed, and the results are illustrated in Fig. 12. The comparison of dynamic behavior of rotating blade with breathing crack under mono- and multi-excitation frequencies are illustrated in Figs. 13 and 14.

A general phenomenon can be observed from Fig. 12 that, besides the primary resonance, the weak second-order super-harmonic resonances are excited within the sub-critical ($\frac{1}{2}f_c$) speed region, which indicates that super-harmonic resonance may serve as an indicator for the presence of crack. However, different crack parameters may lead to different dynamic behavior, as shown in Figs. 12(a)–12(c). By comparing Figs. 12(b) and 12(c), it is suggested that peaks of both primary resonance and super-harmonic resonance get weakened by the decrease of relative crack depth. The comparison of Figs. 12(b) and 12(c) reveals that nonlinear effects of the crack close to blade tip is much weaker than that of the crack nearby the blade root. These comparative results indicate that the crack which is deeper and closer to blade root will be much more dangerous than the one which is shallower and nearer to blade tip. Moreover, under the condition ($\gamma = 0.5$, $\zeta = 1/3$), the weak third-order super-harmonic resonance can be observed, as shown in Fig. 12(b), but disappears in other two conditions (see Figs. 12(a) and 12(c)). It is implicated that the presence of $3\times$ components and the third-order super-harmonic resonance offers a potential indicator for severe crack faults detection. The finding of the second- and third-order super-harmonic resonances under rotating condition is consistent the results of Ref. [52] obtained by analyzing the run-up vibration responses of rotating cracked blade with finite element analysis. These phenomena will be further analyzed in the following context.

According to Ref. [47], if the engine order is an integer (i.e., $EO \in \mathbb{Z}^+$), synchronous vibrations are excited; otherwise, if the engine order is a non-integer (i.e., $EO \in \mathbb{R}^+ \cap EO \notin \mathbb{Z}^+$), asynchronous vibrations are excited. In Fig. 13, only mono-frequency excitation and is considered. The synchronous vibrations are excited since integer engine orders are involved in these cases. Only periodic motions can be observed from Fig. 13. In sub-critical speed region (see Fig. 13(a), $EO = 1$), periodic-2 motion occurs and an obvious $2\times$ component can be obviously observed because of the super-harmonic resonance. Besides, a weak $3\times$ components is also observed in the spectrums. However, in other cases, only weak $2\times$ and $3\times$ components can be observed, and the blade is in periodic-1 motion. Compared with the responses under mono-frequency excitation, the responses under multi-frequency excitation are much more sophisticated, as shown in Fig. 14. Because of the frequency modulation caused by crack closing effect, obvious combination frequencies can be observed in the spectrums. From the phase portraits, it is found that the rotating cracked blade operates at periodic motion if the multi-frequency force only contains integer *EO*, but the periodic motion will switch to quasi-periodic motion if the multi-frequency force contains non-integer *EO*. These results indicate that multi-frequency excitation, especially when it contains non-integer *EO*, will be more dangerous than mono-frequency excitation for rotating cracked blade.

Furthermore, by comparing the spectrum of displacement and velocity, it comes to an important conclusion that the NDI of velocity is much larger than the NDI of displacement. For example, when $EO = 1$, $h_r^{\text{velocity}} = 0.9763$, while $h_r^{\text{displacement}} = 0.4874$. It is indicated that the velocity is much more sensitive than the displacement to the crack closing effect. Further comparison between the NDI of displacement and velocity is illustrated in Fig. 15.

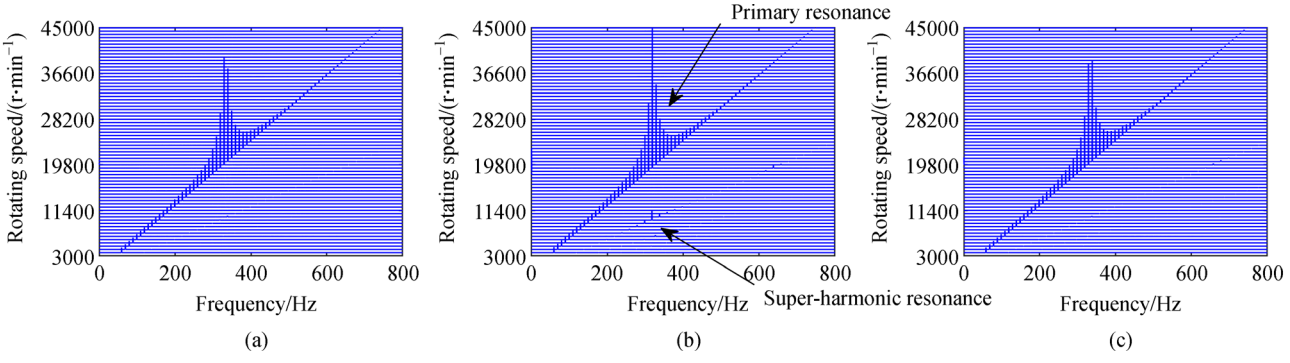

Fig. 12 Spectrum cascades under different rotating speeds when (a) $\gamma = 0.3$, $\zeta = 1/3$; (b) $\gamma = 0.5$, $\zeta = 1/3$; and (c) $\gamma = 0.5$, $\zeta = 2/3$.

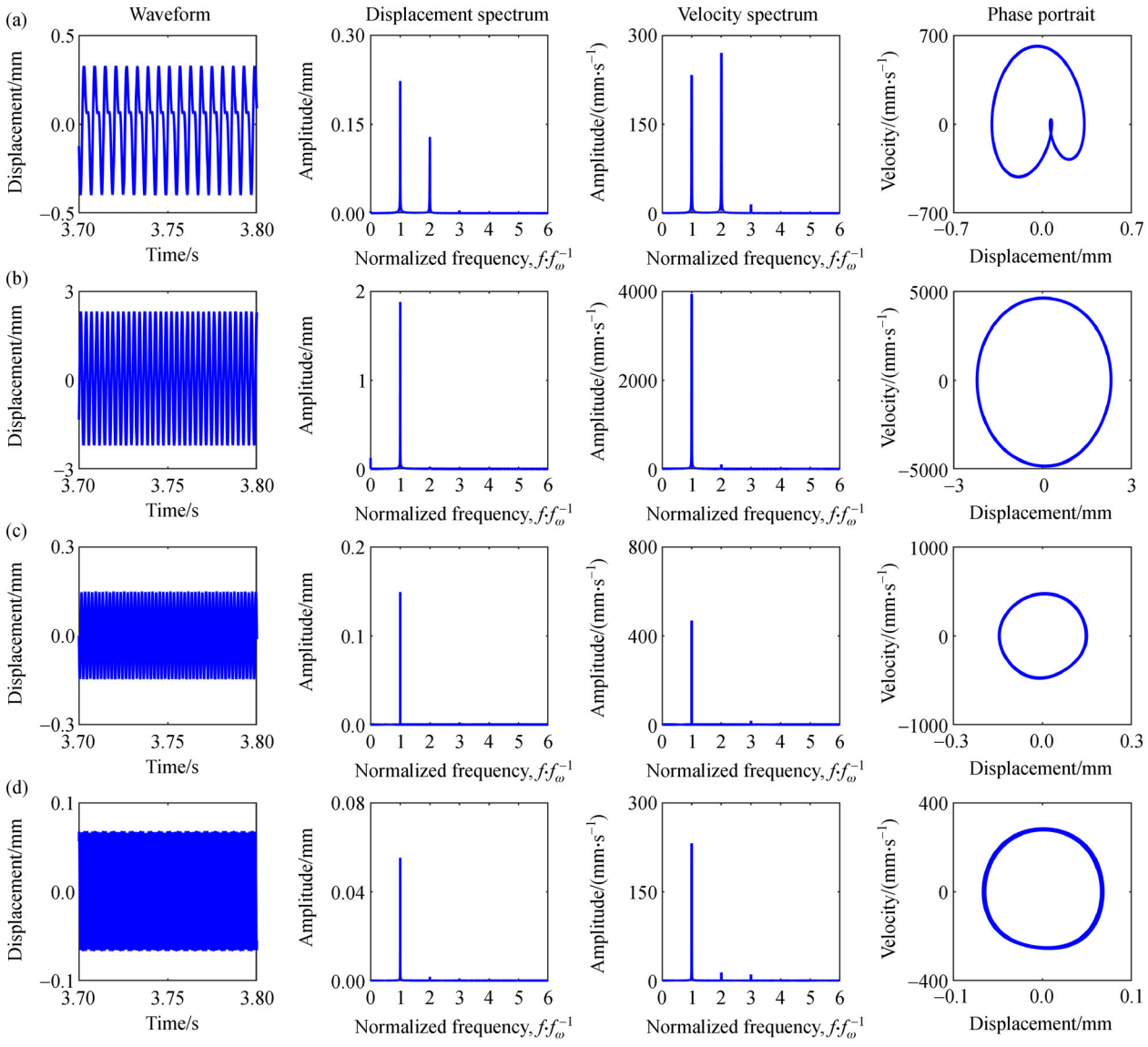

Fig. 13 Synchronous vibration responses under different excitation frequencies: (a) $EO = 1$, (b) $EO = 2$, (c) $EO = 3$, and (d) $EO = 4$.

The comparative results manifest that the NDI of velocity is larger than the one of displacement under all conditions, which verifies the implication obtained from Fig. 13. It is worth further attention that the NDI shown in Fig. 15 makes it more clearly to observe the super-harmonic than spectrums shown in Fig. 12. As shown in Fig. 15, the second-order super-harmonic resonance predominant in the NDI of 2× components, while the third-order super-harmonic resonance predominant in the NDI of 3× components.

4.1.2 Summary of the effects of excitation loads

The effects of load parameters on the vibration responses of NRCBM are analyzed. Some typical features are summarized as follows:

1) The presence of crack will result in the second-order super-harmonic resonance; for some dangerous cases, the third-order super-harmonic resonance may also be induced. These phenomenon offers a potential indicator for the detection of severe crack in rotating blade.

2) Under mono-frequency excitation or multi-frequency excitation only containing integer *EO*, the motion of rotating cracked blade is always periodic, but it turns into quasi-periodic if the system is excited by the multi-frequency excitation containing non-integer *EO*. It is indicated that, multi-frequency excitation, especially when it contains non-integer *EO*, will be more dangerous than mono-frequency excitation for rotating cracked blade.

3) The NDI can better characterize the super-harmonic resonance of NRCBM, as shown in Fig. 15. It is worth noting that the NDI of velocity is much larger than the NDI

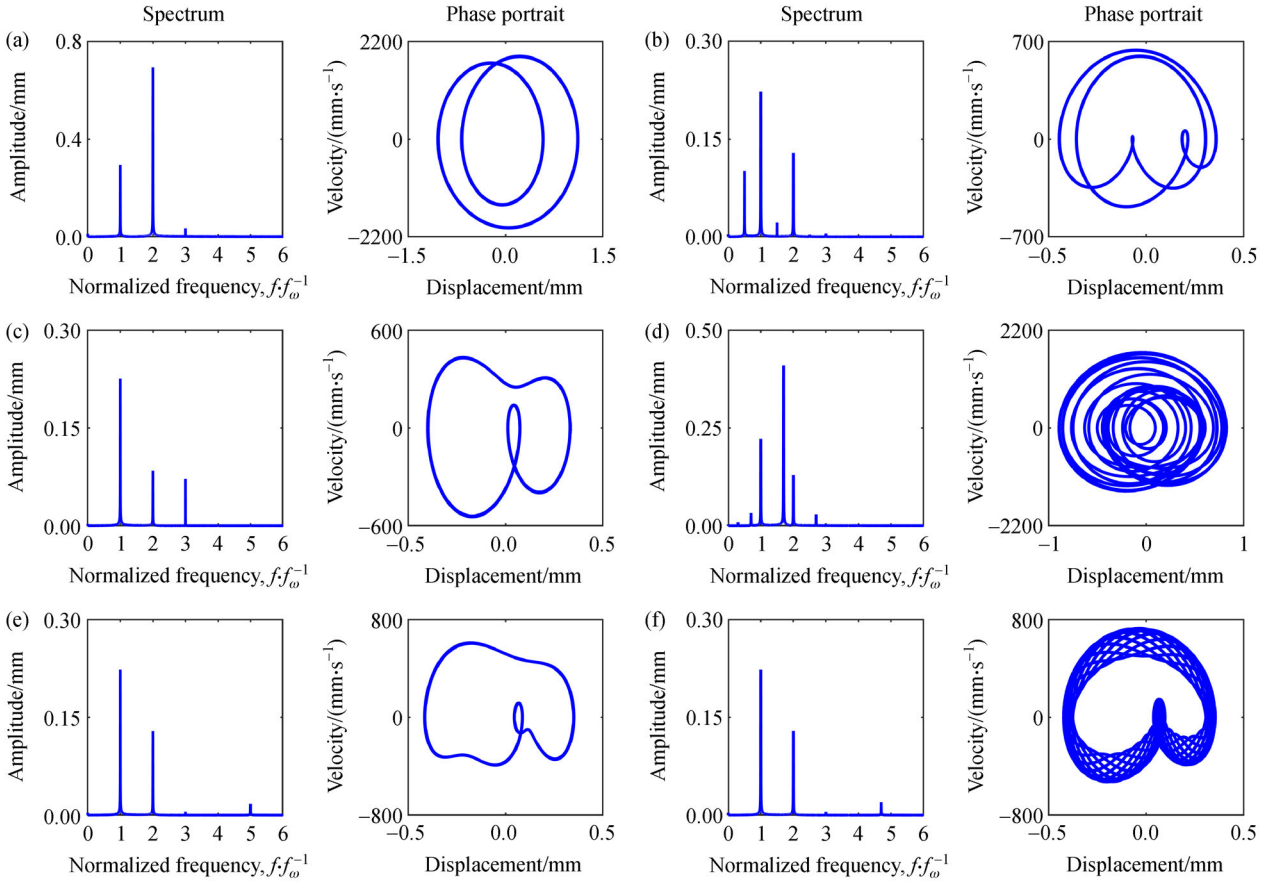

Fig. 14 Vibration responses under different multi-frequency excitation: (a) $EO + 2EO$, (b) $EO + 0.5EO$, (c) $EO + 3EO$, (d) $EO + 1.7EO$, (e) $EO + 5EO$, and (f) $EO + 4.7EO$.

of displacement, especially in $\frac{1}{2}f_c$ and $\frac{1}{3}f_c$ sub-critical region, which indicates that the velocity will be more sensitive to crack breathing effect than the displacement be.

4.2 Effect of crack parameters

In this section, the effects of crack parameters including both relative crack depth and location the nonlinear vibration of rotating cracked blade are explored.

4.2.1 Case 2: Effects of relative crack depth

In this section, the effects of the dimensionless relative crack depth γ on the nonlinear dynamic behavior of NRCBM are investigated. γ changes from 0.1 to 0.5 with an interval of 0.05 and other simulation parameters adopted in this case are shown in Table 5. The AFRs are utilized to present the overall nonlinear dynamic behavior of NRCBM, as shown in Fig. 16. From Fig. 16, following conclusions can be drawn that:

1) Generally, the primary resonant frequency decreases with the increase of relative crack depth, and the primary resonant frequency for the crack near the blade root (see Fig. 16(a), $\zeta = 1/3$) decreases faster than that for the crack close to the blade tip (see Fig. 16(a), $\zeta = 2/3$). It is worth noticing that, when $\zeta = 1/3$), the primary resonant frequency decreases from 335.5 ($\gamma = 0.10$) to 318 Hz ($\gamma = 0.50$) as γ increases from 0.1 to 0.5 (see Fig. 16(a)), which is consistent with the results shown in Table 3.

2) The second-order super-harmonic resonance appears in $\frac{1}{2}f_c$ sub-critical region (see Figs. 16(c) and 16(d)) and the resonance peaks decreases with the decreasing γ. When $\gamma < 0.20$, the resonance peak is so small that it is hard to be observed.

To further analyze the effects of relative crack depths on the nonlinear responses, the spectrum cascades under $EO = 1, 2, ..., 4$ are presented in Fig. 17, and the phase portraits obtained with different relative crack depths are shown in Fig. 18. The results from Fig. 17 indicate that the $2\times$ super-harmonic component appears in the spectrum when $\gamma \geqslant 0.15$ and $EO = 1$, and the amplitudes increases with the increasing γ. This phenomenon can be further

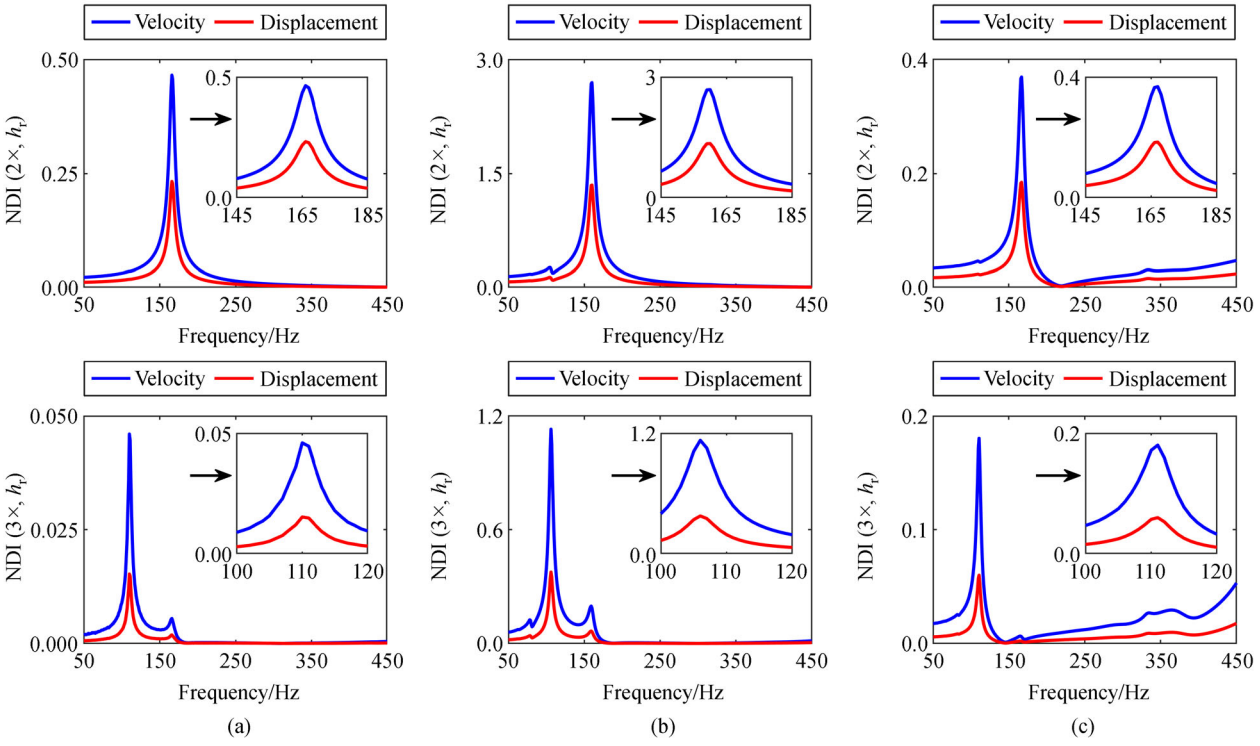

Fig. 15 NDIs of displacement and velocity in sub-critical region under different crack parameters: (a) $\gamma = 0.3$, $\zeta = 1/3$; (b) $\gamma = 0.5$, $\zeta = 1/3$; and (c) $\gamma = 0.5$, $\zeta = 2/3$. NDI: Nonlinear damage indicator.

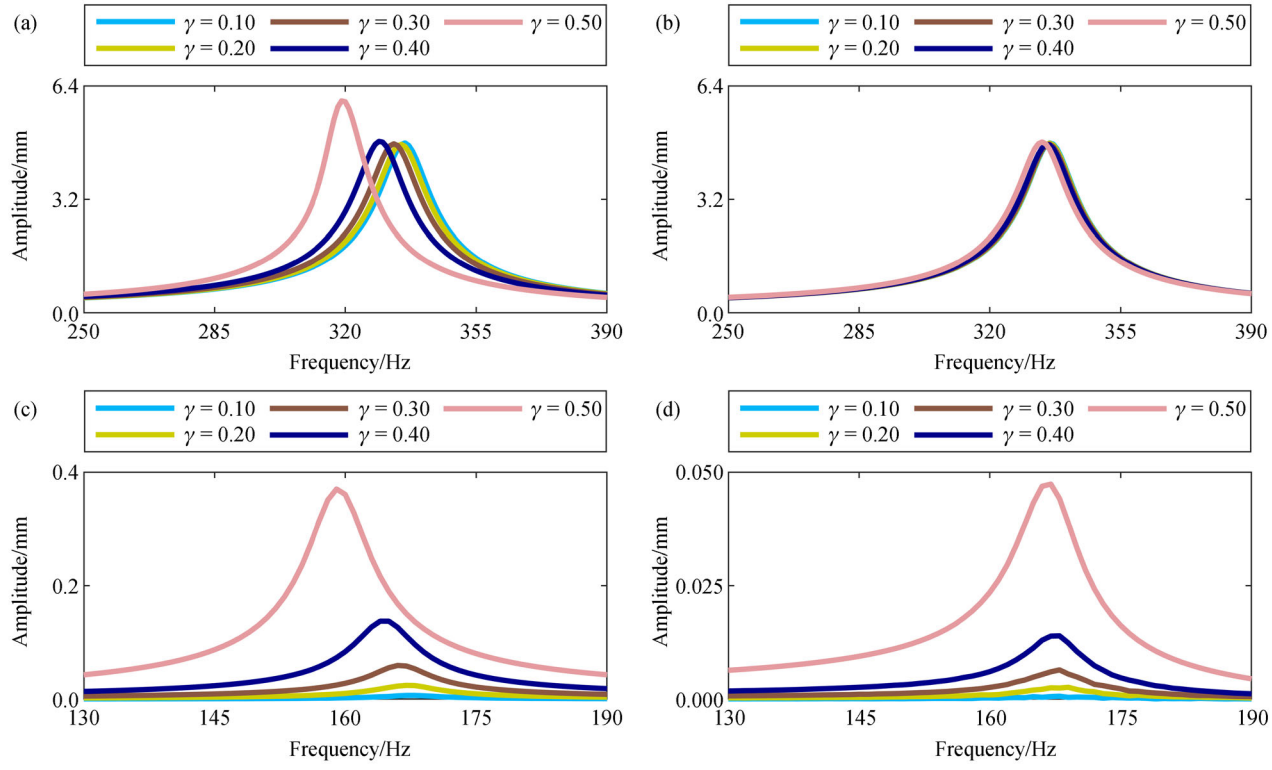

Fig. 16 AFRs for different relative crack depths. (a) Primary resonant region when $\zeta = 1/3$; (b) sub-critical region when $\zeta = 1/3$; (c) primary resonant region when $\zeta = 2/3$; (d) sub-critical region when $\zeta = 2/3$. AFR: Amplitude–frequency responses.

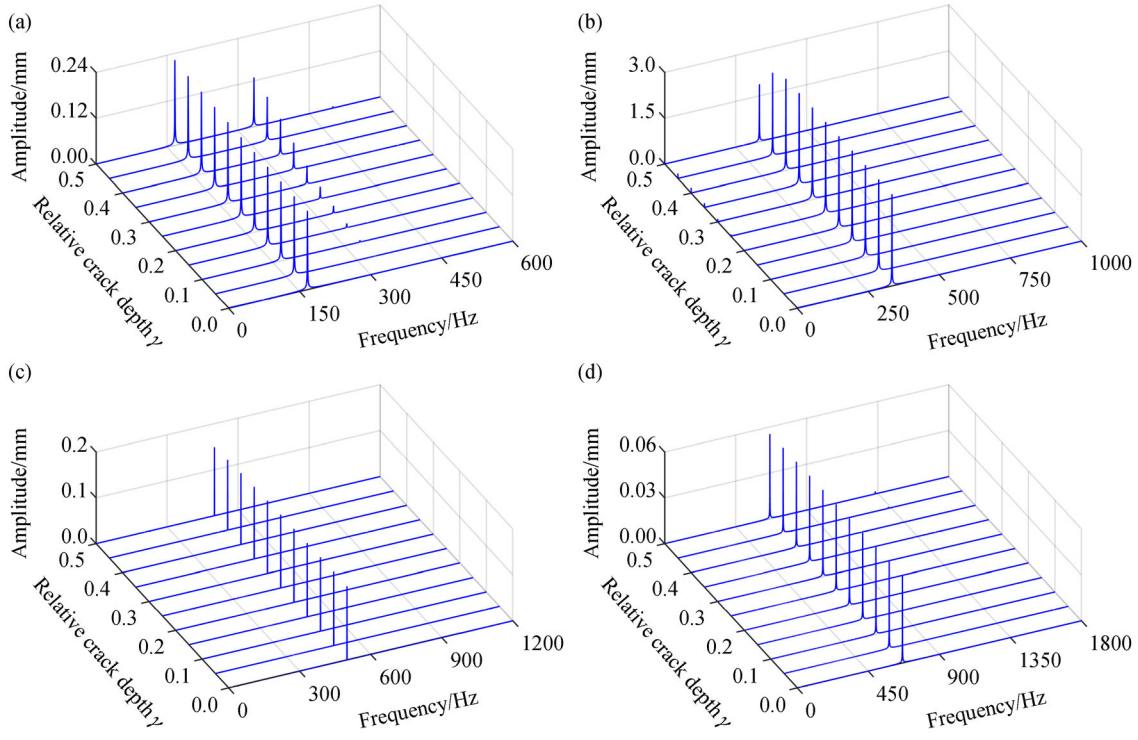

Fig. 17 Spectrum cascades for rotating blade with crack in different relative crack depths when (a) $EO = 1$; (b) $EO = 2$; (c) $EO = 3$; and (d) $EO = 4$.

accounted for in Fig. 18, which indicates the state of NRCBM switches from periodic-2 to periodic-1 motion under $EO = 1$ when the crack depth increases from 0.1 to 0.5.

To further illustrate the significant level of the sub- and super-harmonic components, the NDIs of displacements under $EO = 1$ are obtained, as shown in Fig. 19. It is suggested that the NDI of 2× super-harmonic component in sub-critical region increases with the increase of increasing relative crack depth. When the crack is relatively shallow, i.e., incipient, it is pretty hard to observe 3× or higher-order components. However, as the crack propagates to a very large depth, i.e., γ>0.4, weak 3× appears. This phenomenon is consistent with the analysis in Section 4.1.

4.2.2 Case 3: Effects of relative crack location

In this case, the effects of the dimensionless relative crack location ζ on the nonlinear behavior of NRCBM are investigated. ζ changes from 0.1 to 0.9 with an interval of 0.05 and other simulation parameters adopted in this case is shown in Table 5. The AFR is utilized to present the overall nonlinear dynamic behavior of NRCBM, as shown in Fig. 20. From Fig. 20, following conclusions can be drawn that:

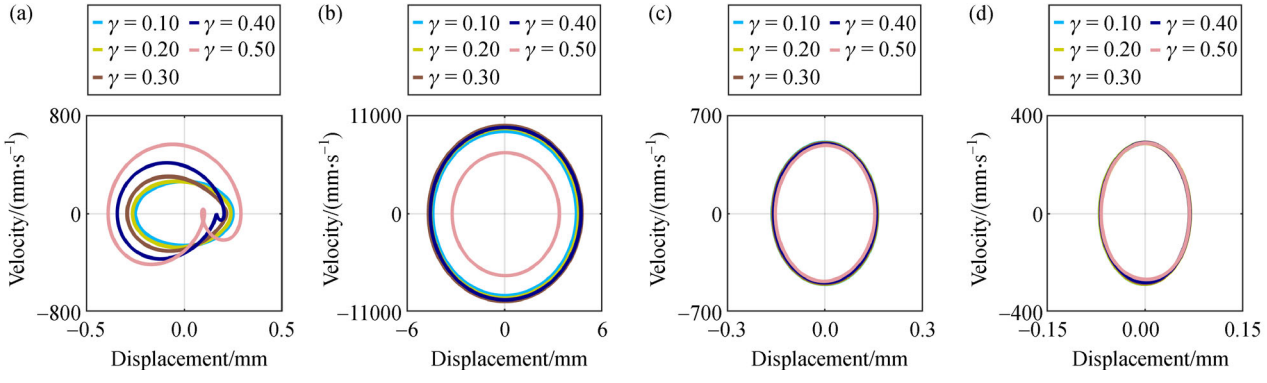

Fig. 18 Phase portraits under different relative crack depths ($\zeta = 1/3$). (a) $EO = 1$; (b) $EO = 2$; (c) $EO = 3$; and (d) $EO = 4$.

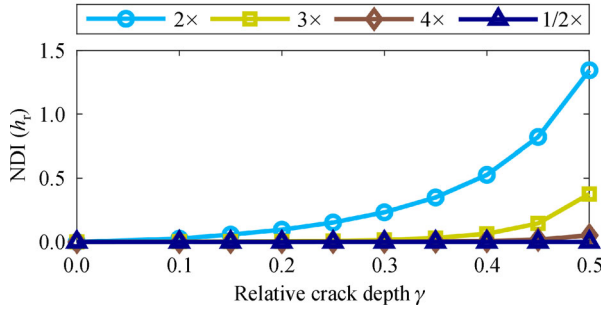

Fig. 19 The variation of NDIs with the change of relative crack depth γ. NDI: Nonlinear damage indicator.

1) Generally, the primary resonant frequency increases with the increase of relative crack location and the larger the relative crack depth is the increasing speed is, as shown in Figs. 20(a) and 20(b). It is worth noting that, when $\gamma = 0.50$, the primary resonant frequency increases from 285 to 336 Hz as ζ increases from 0.10 to 0.90, which matches the results shown in Table 3.

2) Super-harmonic resonance appears in $\frac{1}{2}f_c$ sub-critical region (see Figs. 20(c) and 20(d)). When $\gamma = 0.30$, the resonance peak is so small that is hard to be observed. It is observed that the frequency of super-harmonic resonant peak increases with the increasing ζ.

To further analyze the effects of relative crack locations on the nonlinear responses, the spectrums cascades under $EO = 1, 2, ..., 4$ are shown in Fig. 21, respectively. The phase portraits are displayed in Fig. 22. The comparative results in Fig. 21 suggest that 2× super-harmonic component appears in the spectrums when $\zeta \leqslant 0.75$ and $EO = 1$. Under $EO = 2$ and $EO = 4$, no obvious sub- or super-harmonic components occurs in the spectrums. As ζ increases, the amplitudes of basic harmonic components under sub- ($EO = 1$) and super-critical regions ($EO = 3$ and $EO = 4$) almost remain constant; however, the amplitudes of both 2× super-harmonic components ($EO = 1$) decreases. This is because the nonlinear effects of breathing crack are reduced as crack get closer to the blade tip. This phenomenon can be further accounted for in Fig. 22, which indicates the state of NRCBM switches from periodic-2 to periodic-1 motion under $EO = 1$ when the relative crack location increases from 0.1 to 0.9.

The NDIs for the sub- and super-harmonic components are selected to further analyze the sensitivity of the nonlinear responses to relative crack locations. The results are shown in Fig. 23. It is indicated that both the 2× super-harmonic component in sub-critical region ($\frac{1}{2}f_c$, 10000 r/min) are much more significant than other components. Moreover, it is worth noting that it is hard to observe the second-order super-harmonic resonance from the NDI of 2× super-harmonic component when the crack is very close to blade tip. With the decrease of ζ, the NDI of 2×

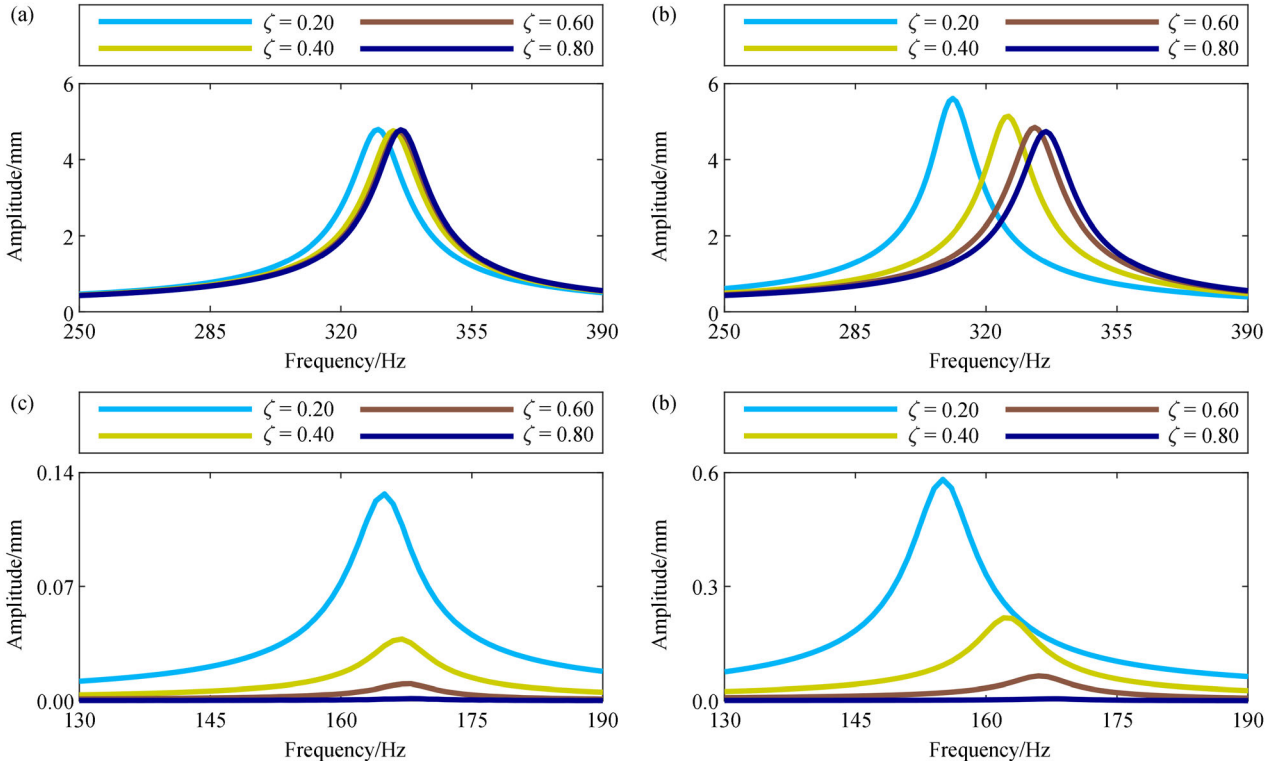

Fig. 20 AFRs for different relative crack locations: (a) Primary resonant region when $\zeta = 0.30$, (b) sub-critical region when $\zeta = 0.30$, (c) primary resonant region when $\zeta = 0.50$, and (d) sub-critical region when $\zeta = 0.50$. AFR: Amplitude–frequency responses.

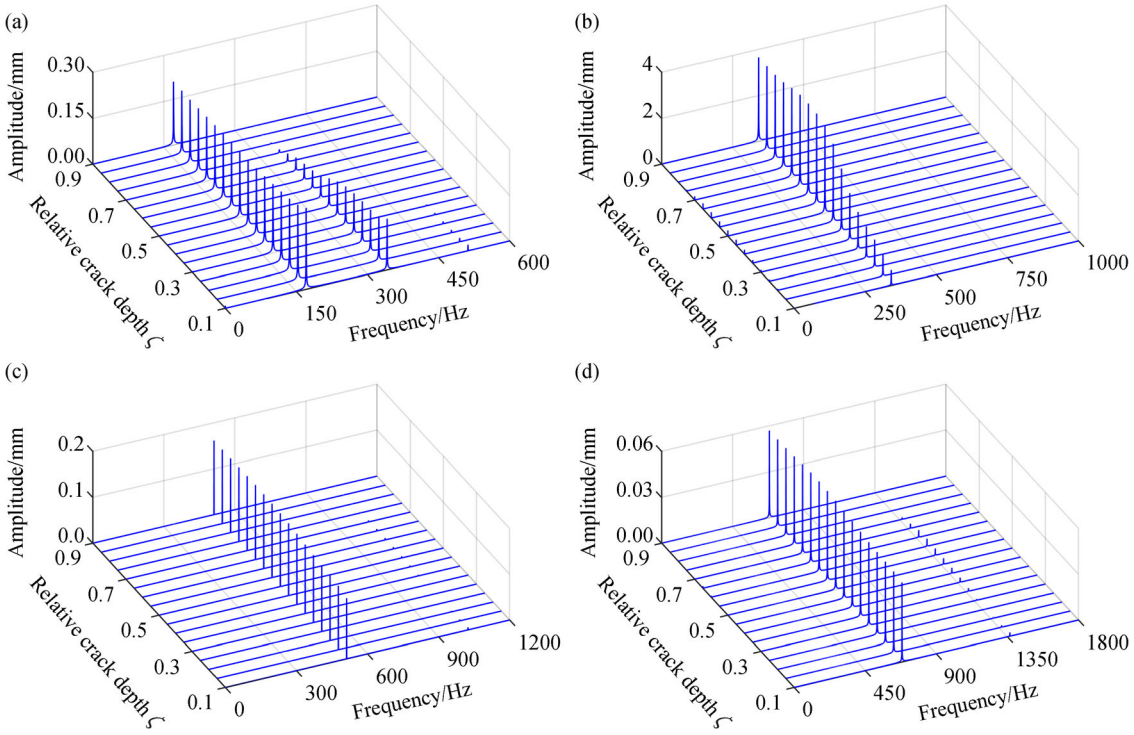

Fig. 21 Spectrum cascades for rotating blade with crack in different locations when (a) $EO = 1$, (b) $EO = 2$, (c) $EO = 3$, and (d) $EO = 4$.

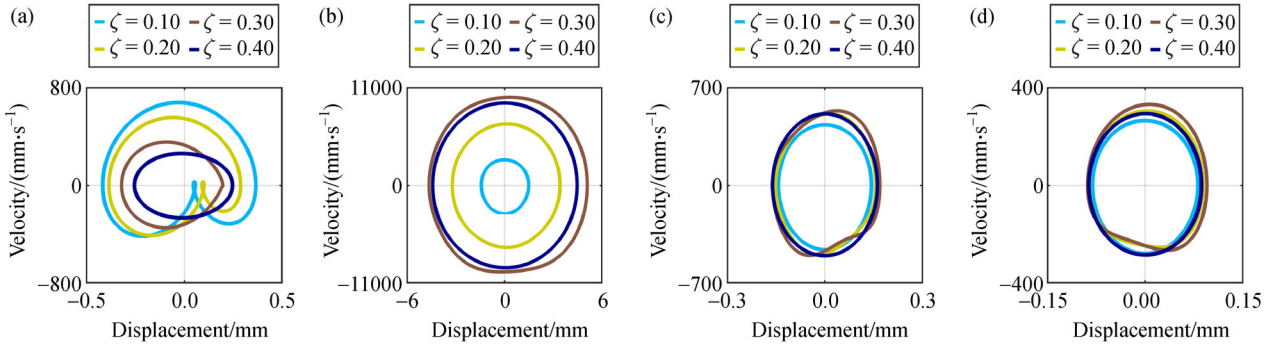

Fig. 22 Phase portraits under different relative crack locations. (a) $EO = 1$; (b) $EO = 2$; (c) $EO = 3$; and (d) $EO = 4$.

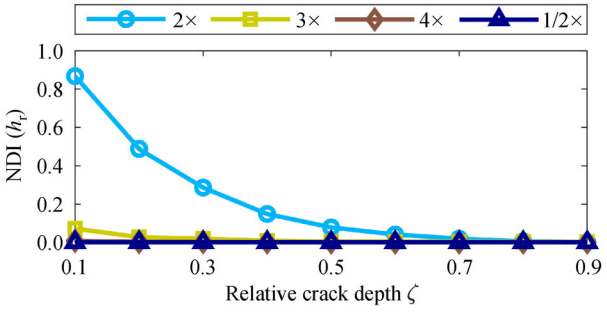

Fig. 23 NDIs of the displacement under different relative crack locations. NDI: Nonlinear damage indicator.

increases, which indicates that the nonlinearity is reduced with the increasing ζ.

4.2.3 Summary of the effects of crack parameters

The crack parameters, including the relative crack depth and relative crack location, on the vibration responses of NRCBM are analyzed. Some typical features are summarized as follows:

1) The nonlinear dynamic behavior is significantly affected by the relative crack depth and relative crack location. Increasing the relative crack depth or the decreasing relative crack location will result in the decrease of the primary resonant frequency, as indicated

in Table 3, and Figs. 16 and 20. By comparing the AFRs when $\zeta = 1/3$ (Figs. 16(a) and 16(c)) and $\zeta = 2/3$ (Figs. 16(b) and 16(d)), it is worth noting that effects of relative crack depths on the nonlinear responses will be reduced for a crack closer to the blade tip. The same conclusion that the effects of relative crack locations on the nonlinear responses will be weaken for a shallow relative crack depth is drawn through the comparison of the AFRs when $\gamma = 0.3$ (Figs. 20(a) and 20(c)) and $\gamma = 0.5$ (Figs. 20(b) and 20(d)).

2) The synchronous vibrations of the rotating blade with different crack parameters are analyzed. The comparative results suggest that the rotating cracked blade will switch from periodic-1 motion to periodic-2 motion when the relative crack depth changes from 0.1 to 0.5 or the relative crack location changes from 0.9 to 0.1. This phenomenon is attributed to the reason that the second-order super-harmonic resonance becomes obvious with the increasing relative crack depth and decreasing relative crack locations. Correspondingly, the NDI of $2\times$ component also shows a tendency to increase with the increase of relative crack depth and the decrease of relative crack location. It is indicated that the crack with larger depth and smaller location will be much more dangerous than the crack with smaller depth and larger location.

5 Discussions of limitations of the proposed method

The main limitation of the proposed method is that the coupling effects among the shaft, disk and blade are neglected. As mentioned in Ref. [12], the coupling vibration among shaft, disk and blades could be significant if the shaft and disk are flexible and blade's stagger angle varies. For high efficiency and productivity purpose, reducing the weight of rotor systems is considered as one of the most efficient way to meet the requirements of high thrust-weight ratio for gas turbines. Both shafts and disks become more and more thin, which results in non-negligible flexibility. It is, therefore, necessary to consider the coupling vibration shaft, disk, and blade. Moreover, this study focusses on the effects of breathing crack on a single blade, thus blade–blade coupling vibration are not considered. The presence of crack will naturally break the tuning property of the periodic grouped-blade structure, leading to vibration localization and further mistuning of the periodic structure, which are also neglected. In addition, the blade may be designed to be pre-twist and installed with a stagger angle, which may also affect its nonlinear dynamic behavior. The effects of pre-twist and stagger angle on the nonlinear vibration of NRCBM are not modeled in this study. Another limitation of NRCBM is that cosine-breathing function increases the simulation accuracy compared to BM, but it cannot clearly characterize the detail of the contact behavior at crack section. These topics will be investigated and coming soon in our future works.

6 Conclusions

A nonlinear dynamic model of rotating cracked blade (NRCBM) is developed on the basis of Euler beam theory to research the nonlinear dynamics of rotating blade with transverse crack. The validity of the proposed NRCBM is verified by using FECCM. The effects of load parameters and crack parameters on the nonlinear dynamic behavior of rotating cracked blade are investigated. The main findings of the study can be summarized as follows:

1) The presence of crack is expected to result in the decrease of resonant frequencies for rotating blade and induce super-harmonic resonance, such as the second- and third-order super-harmonic resonances. The results suggest that the severer the crack is (i.e., a closer crack position to blade root as well as larger relative crack depth), the lager the resonant frequency shifts and the more obvious the super-harmonic resonance presents. The second-order super-harmonic resonance is verified to be more sensitive and distinct than the third-order super-harmonic resonance, and thus may serve as an indicator to diagnose the crack existence. It is worth noting that the third-order super-harmonic resonance only appears for a rotating blade with severe crack, which indicates the third-order super-harmonic resonance offers a potential characteristic signal for severe crack detection and can be utilized to estimate the severity of crack.

2) NDI is verified to be a distinguishable indicator for the severity level estimation of the crack in rotating blade. A significant finding is that the NDI of velocity is much more sensitive to the super-harmonic resonance in sub-critical speed region than the NDI of displacement be. The NDI of $2\times$ super-harmonic components is also found to increase with the increasing crack severity, i.e., the increasing relative crack depth (γ) and the decreasing relative crack location (ζ).

Acknowledgements This work was sponsored by the National Major Project of China (Grant No. 2017-V-0009) and the National Natural Science Foundation of China (Grant No. 51705397). The first author acknowledges the host and support from the Structural Dynamics and Acoustic Systems Laboratory at the University of Massachusetts Lowell, USA.

Appendixes

Appendix A: Matrices and vectors related to the blade

(1) $\boldsymbol{q} \in \mathbb{R}^{2N\times 1}$ is the canonical coordinates vector of the blade, where

$$\boldsymbol{q} = [U_1,\ ...,\ U_i,\ ...,\ U_N,\ V_1,\ ...,\ V_i,\ ...,\ V_N]^{\mathrm{T}},$$

$$(i = 1,\ 2,\ ...,\ N)$$

(2) The mass matrix $\boldsymbol{M} \in \mathbb{R}^{2N\times 2N}$ is

$$\begin{cases} \boldsymbol{M}_{\mathrm{b}}(i,\ j) = \int_0^L \rho A \phi_{1i}(x)\phi_{1j}(x)\mathrm{d}x, \\ \boldsymbol{M}_{\mathrm{b}}(i+N,\ j+N) = \int_0^L \rho A \phi_{2i}(x)\phi_{2j}(x)\mathrm{d}x, \end{cases}$$

where $i,\ j = 1,\ 2,\ ...,\ N$.

(3) The Coriolis force matrix of the blade is denoted by $\boldsymbol{G}_{\mathrm{b}} \in \mathbb{R}^{2N\times 2N}$, which can be expressed as

$$\begin{cases} \boldsymbol{G}_{\mathrm{b}}(i,\ j+N) = -2\Omega\int_0^L \rho A \phi_{2i}(x)\phi_{1j}(x)\mathrm{d}x, \\ \boldsymbol{G}_{\mathrm{b}}(i+N,\ j) = 2\Omega\int_0^L \rho A \phi_{1i}(x)\phi_{2j}(x)\mathrm{d}x, \end{cases}$$

where $i,\ j = 1,\ 2,\ ...,\ N$.

(4) The structural stiffness matrix $\boldsymbol{K}_{\mathrm{e}} \in \mathbb{R}^{2N\times 2N}$ is

$$\begin{cases} \boldsymbol{K}_{\mathrm{e}}(i+N,\ j) = -\int_0^L EA\phi''_{1i}(x)\phi_{1j}(x)\mathrm{d}x, \\ \boldsymbol{K}_{\mathrm{e}}(i,\ j+N) = \int_0^L EI\phi^{(4)}_{2i}(x)\phi_{2j}(x)\mathrm{d}x, \end{cases}$$

where $i,\ j = 1,\ 2,\ ...,\ N$.

(5) The spin softening matrix $\boldsymbol{K}_{\mathrm{so}} \in \mathbb{R}^{2N\times 2N}$ is

$$\boldsymbol{K}_{\mathrm{so}} = -\omega^2 \boldsymbol{M}_{\mathrm{b}}.$$

(6) The centrifugal stiffening matrix $\boldsymbol{K}_{\mathrm{st}} \in \mathbb{R}^{2N\times 2N}$ is

$$\boldsymbol{K}_{\mathrm{st}}(i+N,\ j+N) = -\int_0^L \left(f_{\mathrm{c}}(x)\phi''_{2i}(x) + f'_{\mathrm{c}}(x)\phi'_{2i}(x)\right)\phi_{2j}(x)\mathrm{d}x$$

$$(i,\ j = 1,\ 2,\ ...,\ N).$$

(7) $\boldsymbol{K}_{\mathrm{acc}} \in \mathbb{R}^{2N\times 2N}$ is the stiffness matrix induced by blade acceleration

$$\begin{cases} \boldsymbol{K}_{\mathrm{acc}}(i,\ j+N) = -\int_0^L \rho A\dot{\Omega}\phi_{2i}(x)\phi_{1j}(x)\mathrm{d}x, \\ \boldsymbol{K}_{\mathrm{acc}}(i+N,\ j) = \int_0^L \rho A\dot{\Omega}\phi_{1i}(x)\phi_{2j}(x)\mathrm{d}x, \end{cases}$$

where $i,\ j = 1,\ 2,\ ...,\ N$.

(8) $\boldsymbol{D}_{\mathrm{b}} \in \mathbb{R}^{2N\times 2N}$ is the Rayleigh damping coefficients matrix and can be expressed as

$$\boldsymbol{D}_{\mathrm{b}} = \alpha\boldsymbol{M}_{\mathrm{b}} + \beta\boldsymbol{K}_{\mathrm{b}},$$

where α and β are the structural damping ratio,

$$\begin{cases} \alpha = \dfrac{4\pi f_{\mathrm{n1}} f_{\mathrm{n2}}(f_{\mathrm{n1}}\xi_2 - f_{\mathrm{n2}}\xi_1)}{f_{\mathrm{n1}}^2 - f_{\mathrm{n2}}^2}, \\ \beta = \dfrac{f_{\mathrm{n2}}\xi_2 - f_{\mathrm{n1}}\xi_1}{\pi(f_{\mathrm{n2}}^2 - f_{\mathrm{n1}}^2)}, \end{cases}$$

where f_{n1} and f_{n2} denote the first and second natural frequency of the static blade, respectively, and $\xi_1 = 0.0268$ and $\xi_2 = 0.0536$ correspond to the modal damping ratio, respectively.

(9) The external force vector $\boldsymbol{F} \in \mathbb{R}^{2N\times 1}$ is

$$\begin{cases} \boldsymbol{F}(j,\ 1) = \int_0^L \rho A\Omega^2(x + R_{\mathrm{d}})\phi_{1j}(x)\mathrm{d}x, \\ \boldsymbol{F}(j+N,\ 1) = -\int_0^L \rho A\dot{\Omega}(x + R_{\mathrm{d}})\phi_{2j}(x)\mathrm{d}x \\ +\int_x^L f_{\mathrm{e}}(x,\ t)\phi_{2j}(x)\mathrm{d}x, \end{cases}$$

where $j = 1,\ 2,\ ...,\ N$.

Appendix B: Matrices and vectors related to the crack

$\boldsymbol{K}_{\mathrm{cr}} \in \mathbb{R}^{2N\times 2N}$ is the stiffness alteration caused by fully "open" crack:

$$\boldsymbol{K}_{\mathrm{c}}(i+N,\ j+N) = 6(1-\nu^2)Q(\gamma)h\int_0^L EI\phi^{(4)}_{2i}(x)\phi_{2j}(x)\delta(x-l_{\mathrm{c}})\mathrm{d}x,$$

where $i,\ j = 1,\ 2,\ ...,\ N$.

References

1. Abdelrhman A M, Leong M S, Saeed S A M, et al. A review of vibration monitoring as a diagnostic tool for turbine blade faults. Applied Mechanics and Materials, 2012, 229–231: 1459–1463
2. Carter T J. Common failures in gas turbine blades. Engineering Failure Analysis, 2005, 12(2): 237–247
3. Yang L, Chen X, Wang S. Mechanism of fast time-varying vibration for rotor–stator contact system: With application to fault diagnosis. Journal of Vibration and Acoustics, 2018, 140(1): 014501
4. Gates D. Rolls-Royce spending millions of dollars to repair 787 engines. Available from The Seattle Times website on 2020-9-14
5. Abdelrhman A M, Hee L M, Leong M, et al. Condition monitoring of blade in turbomachinery: A review. Advances in Mechanical Engineering, 2014, 6(1): 210717
6. Gubran A. Vibration diagnosis of blades of rotating machines. Dissertation for the Doctoral Degree. Manchester: The University of Manchester, 2015
7. Rafiee M, Nitzsche F, Labrosse M. Dynamics, vibration and control of rotating composite beams and blades: A critical review. Thin-Walled Structures, 2017, 119: 795–819
8. Yuan J, Scarpa F, Allegri G, et al. Efficient computational techniques for mistuning analysis of bladed discs: A review. Mechanical Systems and Signal Processing, 2017, 87: 71–90
9. Ma H, Yin F, Guo Y, et al. A review on dynamic characteristics of blade–casing rubbing. Nonlinear Dynamics, 2016, 84: 437–472
10. Wang L, Cao D, Huang W. Nonlinear coupled dynamics of flexible blade–rotor–bearing systems. Tribology International, 2010, 43(4):

759–778
11. Ma H, Lu Y, Wu Z, et al. A new dynamic model of rotor–blade systems. Journal of Sound and Vibration, 2015, 357: 168–194
12. She H, Li C, Tang Q, et al. The investigation of the coupled vibration in a flexible-disk blades system considering the influence of shaft bending vibration. Mechanical Systems and Signal Processing, 2018, 111: 545–569
13. Ma H, Xie F, Nai H, et al. Vibration characteristics analysis of rotating shrouded blades with impacts. Journal of Sound and Vibration, 2016, 378: 92–108
14. Sinha S K, Turner K E. Natural frequencies of a pre-twisted blade in a centrifugal force field. Journal of Sound and Vibration, 2011, 330(11): 2655–2681
15. Oh Y, Yoo H H. Vibration analysis of a rotating pre-twisted blade considering the coupling effects of stretching, bending, and torsion. Journal of Sound and Vibration, 2018, 431: 20–39
16. Batailly A, Meingast M, Legrand M. Unilateral contact induced blade/casing vibratory interactions in impellers: Analysis for rigid casings. Journal of Sound and Vibration, 2015, 337: 244–262
17. Yuan J, Scarpa F, Titurus B, et al. Novel frame model for mistuning analysis of bladed disk systems. Journal of Vibration and Acoustics, 2017, 139(3): 031016
18. Xie F, Ma H, Cui C, et al. Vibration response comparison of twisted shrouded blades using different impact models. Journal of Sound and Vibration, 2017, 397: 171–191
19. Ma H, Lu Y, Wu Z, et al. Vibration response analysis of a rotational shaft–disk–blade system with blade-tip rubbing. International Journal of Mechanical Sciences, 2016, 107: 110–125
20. Tang W, Epureanu B I. Nonlinear dynamics of mistuned bladed disks with ring dampers. International Journal of Non-linear Mechanics, 2017, 97: 30–40
21. Yu P, Zhang D, Ma Y, et al. Dynamic modeling and vibration characteristics analysis of the aero-engine dual-rotor system with fan blade out. Mechanical Systems and Signal Processing, 2018, 106: 158–175
22. Yang L, Chen X, Wang S. A novel amplitude-independent crack identification method for rotating shaft. Proceedings of the Institution of Mechanical Engineers. Part C, Journal of Mechanical Engineering Science, 2018, 232(22): 4098–4112
23. Chasalevris A C, Papadopoulos C A. Identification of multiple cracks in beams under bending. Mechanical Systems and Signal Processing, 2006, 20(7): 1631–1673
24. Zhang K, Yan X. Multi-cracks identification method for cantilever beam structure with variable cross-sections based on measured natural frequency changes. Journal of Sound and Vibration, 2017, 387: 53–65
25. Li B, Chen X, Ma J, et al. Detection of crack location and size in structures using wavelet finite element methods. Journal of Sound and Vibration, 2005, 285(4–5): 767–782
26. Giannini O, Casini P, Vestroni F. Nonlinear harmonic identification of breathing cracks in beams. Computers & Structures, 2013, 129: 166–177
27. Zeng J, Ma H, Zhang W, et al. Dynamic characteristic analysis of cracked cantilever beams under different crack types. Engineering Failure Analysis, 2017, 74: 80–94
28. Liu J, Shao Y, Zhu W. Free vibration analysis of a cantilever beam with a slant edge crack. Proceedings of the Institution of Mechanical Engineers. Part C, Journal of Mechanical Engineering Science, 2017, 231(5): 823–843
29. Liu J, Zhu W D, Charalambides P G, et al. A dynamic model of a cantilever beam with a closed, embedded horizontal crack including local flexibilities at crack tips. Journal of Sound and Vibration, 2016, 382: 274–290
30. Bovsunovsky A, Surace C. Non-linearities in the vibrations of elastic structures with a closing crack: A state of the art review. Mechanical Systems and Signal Processing, 2015, 62–63: 129–148
31. Douka E, Hadjileontiadis L J. Time–frequency analysis of the free vibration response of a beam with a breathing crack. NDT & E International, 2005, 38(1): 3–10
32. Rezaee M, Hassannejad R. Free vibration analysis of simply supported beam with breathing crack using perturbation method. Acta Mechanica Solida Sinica, 2010, 23(5): 459–470
33. Vigneshwaran K, Behera R K. Vibration analysis of a simply supported beam with multiple breathing cracks. Procedia Engineering, 2014, 86: 835–842
34. Andreaus U, Casini P, Vestroni F. Non-linear dynamics of a cracked cantilever beam under harmonic excitation. International Journal of Non-Linear Mechanics, 2007, 42(3): 566–575
35. Andreaus U, Baragatti P. Cracked beam identification by numerically analysing the nonlinear behaviour of the harmonically forced response. Journal of Sound and Vibration, 2011, 330(4): 721–742
36. Ma H, Zeng J, Lang Z, et al. Analysis of the dynamic characteristics of a slant-cracked cantilever beam. Mechanical Systems and Signal Processing, 2016, 75: 261–279
37. Zhang W, Ma H, Zeng J, et al. Vibration responses analysis of an elastic-support cantilever beam with crack and offset boundary. Mechanical Systems and Signal Processing, 2017, 95: 205–218
38. Liu C, Jiang D. Crack modeling of rotating blades with cracked hexahedral finite element method. Mechanical Systems and Signal Processing, 2014, 46(2): 406–423
39. Kuang J W, Huang B W. Mode localization of a cracked blade-disks. In: Proceedings of the ASME 1998 International Gas Turbine and Aeroengine Congress and Exhibition. Volume 5: Manufacturing Materials and Metallurgy; Ceramics; Structures and Dynamics; Controls, Diagnostics and Instrumentation; Education. Stockholm: ASME, 1998, V005T014A013
40. Huang B W, Kuang J H. Variation in the stability of a rotating blade disk with a local crack defect. Journal of Sound and Vibration, 2006, 294(3): 486–502
41. Panigrahi B, Pohit G. Effect of cracks on nonlinear flexural vibration of rotating Timoshenko functionally graded material beam having large amplitude motion. Proceedings of the Institution of Mechanical Engineers. Part C, Journal of Mechanical Engineering Science, 2018, 232(6): 930–940
42. Kim S S, Kim J H. Rotating composite beam with a breathing crack. Composite Structures, 2003, 60(1): 83–90
43. Xu H, Chen Z, Xiong Y, et al. Nonlinear dynamic behaviors of rotated blades with small breathing cracks based on vibration power flow analysis. Shock and Vibration, 2016, 2016(1): 1–11
44. Xu H, Chen Z, Yang Y, et al. Effects of crack on vibration characteristics of mistuned rotated blades. Shock and Vibration, 2017, 1785759

45. Saito A. Nonlinear vibration analysis of cracked structures: Application to turbomachinery rotors with cracked blades. Dissertation for the Doctoral Degree. Michigan: The University of Michigan, 2009
46. Xie J, Zi Y, Zhang M, et al. A novel vibration modeling method for a rotating blade with breathing cracks. Science China. Technological Sciences, 2019, 62(2): 333–348
47. Jousselin O. Development of blade tip timing techniques in turbo machinery. Dissertation for the Doctoral Degree. Manchester: The University of Manchester, 2013
48. Dimarogonas A D, Paipetis S A, Chondros T G. Analytical Methods in Rotor Dynamics. 2nd ed. Dordrecht: Springer, 2013
49. Tata H, Paris P, Irwin G. The Stress Analysis of Crack Handbook. 3rd ed. New York: ASME Press, 2000
50. Chati M, Rand R, Mukherjee S. Modal analysis of a cracked beam. Journal of Sound and Vibration, 1997, 207(2): 249–270
51. Saito A, Castanier M P, Pierre C. Estimation and veering analysis of nonlinear resonant frequencies of cracked plates. Journal of Sound and Vibration, 2009, 326(3–5): 725–739
52. Zeng J, Chen K, Ma H, et al. Vibration response analysis of a cracked rotating compressor blade during run-up process. Mechanical Systems and Signal Processing, 2019, 118(3): 568–583